NASA Contractor Report 2926

Neutrally Stable Atmospheric Flow Over a Two-Dimensional Rectangular Block

Chih Fang Shieh, Walter Frost,
and Juergen Bitte

CONTRACT NAS8-29584
NOVEMBER 1977

NASA

NASA Contractor Report 2926

Neutrally Stable Atmospheric Flow Over a Two-Dimensional Rectangular Block

Chih Fang Shieh, Walter Frost,
and Juergen Bitte
The University of Tennessee Space Institute
Tullahoma, Tennessee

Prepared for
George C. Marshall Space Flight Center
under Contract NAS8-29584

NASA
National Aeronautics
and Space Administration

**Scientific and Technical
Information Office**

1977

AUTHORS' ACKNOWLEDGMENTS

The work reported herein was supported by the National Aeronautics and Space Administration, Marshall Space Flight Center, Space Sciences Laboratory, Atmospheric Sciences Division, under contract number NAS8-29584.

The authors are indebted to Mr. William A. McGowan of the Aviation Safety Technology Branch, Office of Advanced Research and Technology (OAST), NASA Headquarters, Washington, D. C., for his support of this research. Special thanks also go to Dr. G. H. Fichtl and Mr. Dennis Camp of the Marshall Space Flight Center who were the scientific monitors of the program.

TABLE OF CONTENTS

LIST OF FIGURES

FIGURE PAGE

NOMENCLATURE

a,b,c	Coefficient functions in the general elliptic equation (Equation 13)
C_μ	Empirical function in expression for effective viscosity (Equation 17)
C_D	Empirical function in source term for turbulence kinetic energy equation (Equation 20)
C_B, C_S	Empirical functions in source term for ℓ-equation (Equation 23)
$C_{\mu\infty}, C_{D\infty}, C_{B\infty}, C_{S\infty}$	Empirical constant for C_μ, C_D, C_B, C_S respectively if R_t is extremely large
d	Source term in general elliptic equation (Equation 13)
H	Height of block
k	von Karman constant (= 0.4)
K	Turbulence kinetic energy; $\frac{1}{2}(\overline{u'^2} + \overline{v'^2} + \overline{w'^2})$
ℓ	Prandtl mixing length or local turbulence length scale
m	Exponent of velocity power law
n	General normal coordinate
Δn	Numerical step size in n-direction
p	Pressure
Ri	Richardson number, ratio of buoyance effects over viscous effects
R_t	Turbulent Reynolds number defined by Equation 24

S_ω, S_k, S_ℓ	Respective source terms in ω-, K- and ℓ-transport equation and defined by Equations 12, 20 and 23
u	Velocity component in x-direction
u_{rms}	Root-mean-square velocity fluctuation in the x-direction
u_*	Friction velocity, $\sqrt{\tau_{wall}/\rho}$
u_0	Local mean velocity in the x-direction in the absence of the block model carried out in References [4, 28]
u_∞	Characteristic velocity defined by Equation 1 at z = 6.0 H
U_∞	Value of u above the boundary layer
w	Velocity component in z-direction
x	Horizontal coordinate
Δx	Numerical step size in x-direction
y	Distance in z-direction measured from axis of mixing layer
z	Vertical coordinate
Δz	Numerical step size in z-direction
z_0	Surface roughness

Greek Symbols

$\Gamma_{k,eff}$	Effective exchange coefficient for turbulence kinetic energy; $\mu_{eff}/\sigma_{k,eff}$
$\Gamma_{\ell,eff}$	Effective exchange coefficient for turbulence length scale; $\mu_{eff}/\sigma_{\ell,eff}$
δ	Boundary layer thickness

μ	Dynamic viscosity of the flow
μ_t	Turbulent viscosity of the flow
μ_{eff}	Effective viscosity; $\mu + \mu_t$
ν	Kinematic viscosity of the flow
β	Parameter used in Hunt's theory ($\beta^{-1} = \frac{\ell n[H/z_0]}{2k^2}$)
η	Parameter used in Hunt's theory ($\eta = \frac{z/H}{[\beta(x/H)]^{1/(m+2)}}$)
ξ	Similarity variable in mixing-layer theory ($= \sigma \frac{y}{x}$)
ρ	Density of the flow
σ	Similarity parameter in mixing layer theory
$\sigma_{k,eff}$	Schmidt number for turbulence kinetic energy based on effective viscosity
$\sigma_{\ell,eff}$	Schmidt number for turbulence length scale based on effective viscosity
σ_u	Velocity deviation in x-direction
σ_v	Velocity deviation in y-direction
σ_w	Velocity deviation in z-direction
τ	Shear stress
τ_{wall}	Shear stress at surface
ϕ	Dependent variable in general elliptic equation (Equation 13)
ψ	Stream function
ω	Vorticity as defined by Equation 9

Superscripts

	Turbulent fluctuation about mean flow quantity

$\bar{}$	Mean flow quantity as ensemble average
N	Index of iteration
Subscripts	
C	Production term in Equations 20 and 23
D	Dissipation term in Equations 20 and 23
eff	Effective transport property, comprising both molecular and turbulent contributions
in	Inflow condition
i, j	Subscripts for Cartesian tensors (i = 1, 2, 3, j = 1, 2, 3)
I	Finite difference index for the x-direction
J	Finite difference index for the z-direction
IN	Finite difference index for the maximum value of I
JN	Finite difference index for the maximum value of J
P	Pertains to node at which dependent variable is currently being calculated
NP	Refers to node lying adjacent to boundary node
ref	General reference condition (page 14)
t	Turbulent flow quantity
ℓ	Local flow quantity

CHAPTER I

INTRODUCTION AND STATEMENT OF PROBLEM

Atmospheric turbulence and mean winds have influenced the design of the control, stability and guidance of aircraft for many years. Recently, the study of atmospheric flow around buildings and other man-made obstructions has attained major importance in the design and operational procedures of helicopter and V/STOL aircraft operating in large metropolitan areas. Such low speed aircraft flying near buildings may experience fields of induced vorticity, zones of recirculation and regions of large fluctuations which can make takeoff and landing extremely hazardous.

Civil engineers are also concerned with unsteady atmospheric flow which induces dynamic loads on structures. Pollution control and monitoring are strongly influenced by the motion of the atmosphere over buildings. Many other areas of current technology also require an understanding of atmospheric flows in the vicinity of buildings. Since full-scale experimental studies of building flow phenomena are costly and exact simulation in wind tunnels remains to be verified the need for analytical methods to predict local atmospheric motion influenced by surface obstructions is thus obvious. The purpose of this study is to develop a meaningful mathematical model of flow over a single two-dimensional block geometry. The problem concerned herein is

the wind field over a rectangular block on a flat plane surface. Undisturbed neutrally stable atmospheric wind perpendicular to the axis of the building is assumed far upstream and far downstream of the obstacle, see Figure 1.

To provide a better understanding of fluid mechanics of the problem, the flow regions associated with bluff body flow are qualitatively discussed in the following. Frost [1] [1] has compiled an extensive survey of flow properties around man-made surface obstructions to the wind. The distorted shear flows approaching and passing over a block geometry can be divided into three basic flow regions, Figure 2: (1) the displacement zone, (2) the upstream separation bubble or downwash zone, and (3) the wake zone which includes the rear separation bubble or cavity zone. The effect of shear in the approaching flow generates a vortex near the ground upstream of the block, creating a downwash on the front face. This can be interpreted as the piling up of vortex lines swept in by the incident flow. Also, shear generates a swirling flow in the wake or cavity zone, which can be explained as the accumulation of vortex lines in the wake zone by the passing flow. When the flow passes over the abrupt change in geometry at the corner of the block surface, separation from the sharp edge occurs. On the forward surface of the block the strong pressure gradient above the region of the separated eddy accelerates the fluid in

---

[1]Numbers in brackets refer to similarly numbered references in the Bibliography.

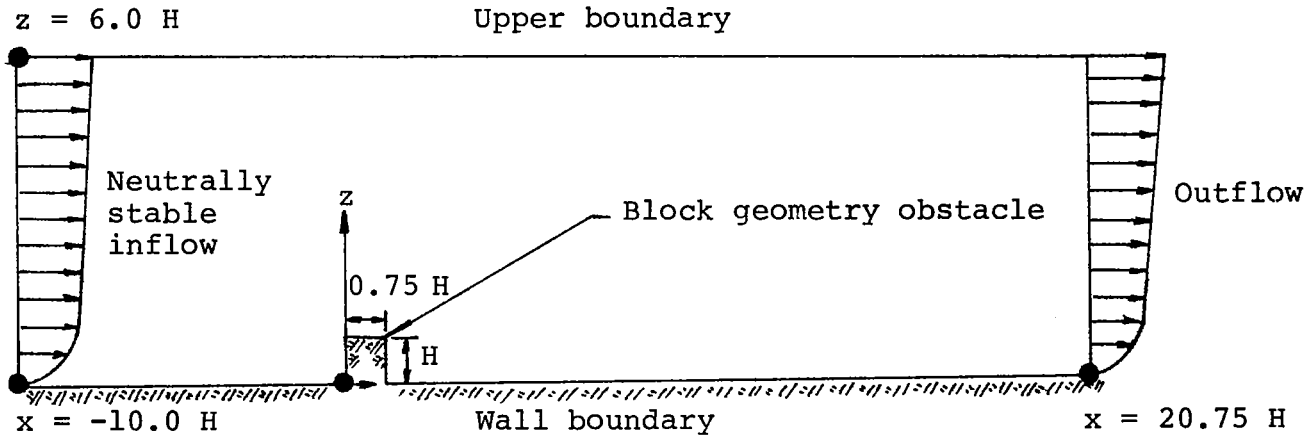

Figure 1. Description of flow region considered.

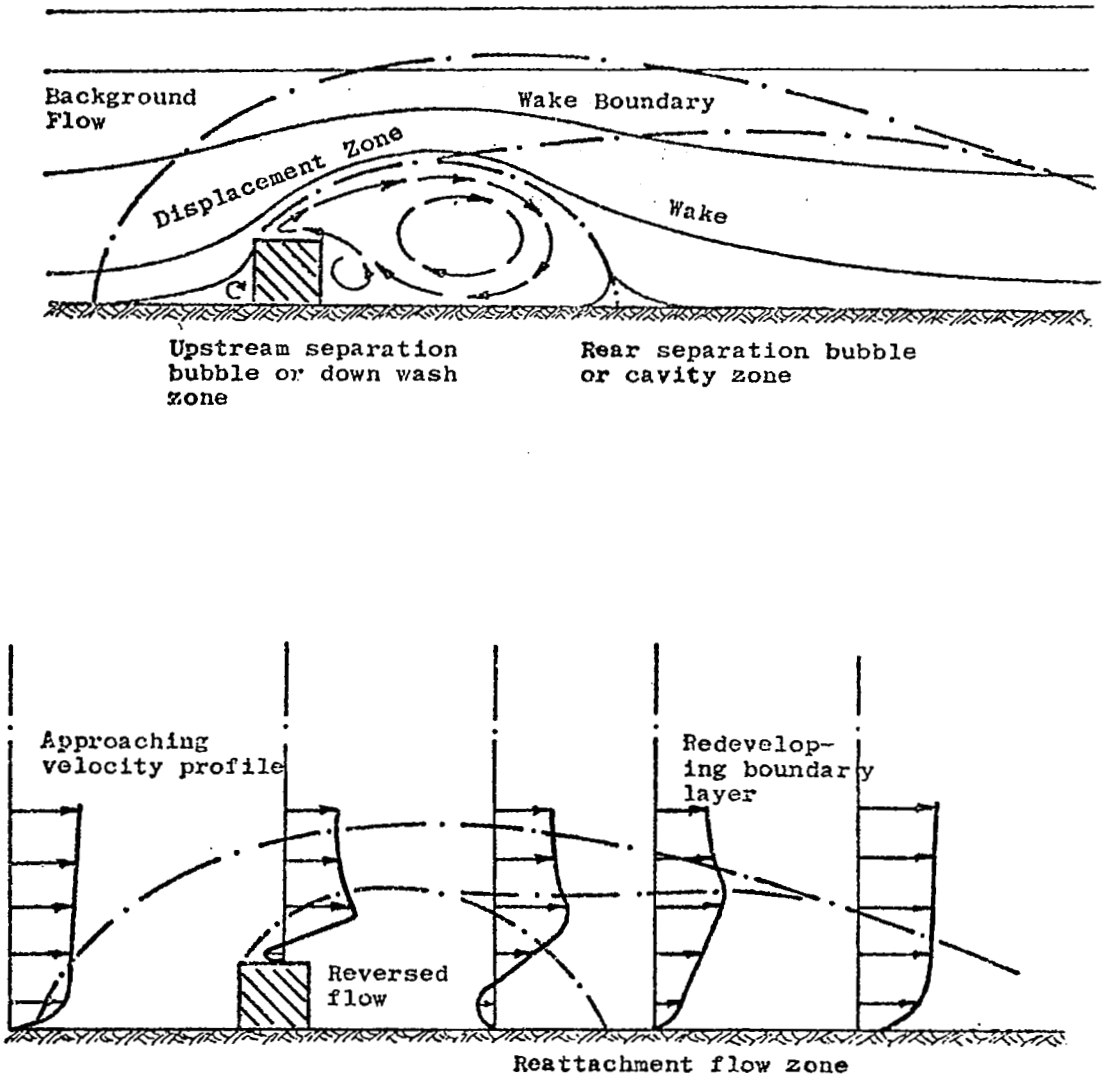

Figure 2. Definition of flow zones near a sharp-edged block [1].

the thin surface boundary layer toward the sharp leading edge where, due to its vertically directed momentum, it is forced to separate. The separated flow forms a shear layer of low static pressure and high vorticity which is bent downstream through interaction with the transverse main flow forming an essential shell which reattaches some distance downstream. The intensity of turbulence in the incident flow tends to force the wake to reattach closer to the back-side of the block and to thicken the shear layer which bounds the wake zone. An adverse pressure gradient and viscosity are two necessary conditions for flow separation to occur on the upstream face [2]. Downstream of separation from the corner momentum in the separated layer diffuses into the wake and into the quasi-potential flow outside the wake setting the wake fluid into motion and smoothing out the sharp velocity discontinuity. Beyond the point of reattachment this diffusion gradually thickens the shear layer until the inner flow is blended with the outer flow forming a new and thicker boundary layer. At the forward separation point and at the reattachment point of the wake where the normal velocity gradient at the surface is zero, the shear stress in laminar flow is reduced to zero. The longitudinal position on the surface where the shear stress becomes zero is identified as the separation point or reattachment point. Experimentally, the above description of zero stress which correlates with the onset of reverse flow is only true for a steady two-dimensional, laminar incompressible flow. For turbulent flow

the zero stress position fluctuates widely. However, ensemble time-average quantities are generally employed such that the mean normal velocity gradient is zero, i.e., the separation point and the reattachment point are assumed to coincide with the condition of zero normal gradient in the mean velocity.

Wakes generated by obstacles are characterized by increased turbulence, a mean velocity defect, and in certain situations by organized, discrete standing vortices. One of the first efforts to determine the characteristics of full-scale building wake was made by Colmer [3]. Colmer drew the conclusion for his study that the mean velocity deficit had completely decayed by 14 obstacle heights downstream and turbulence intensity excess, although small, was still apparent at 14 heights downstream. Frost and Shahabi [5] conducted a field test of wind passing over a simulated rectangular block building and observed that the average midpoint of reattachment along the centerline of the wake was 12.5 ± 2.34 building heights. Typical values measured for two-dimensional bluff bodies in wind tunnels range from 13 to 17 building heights [5]. Lemberg [6] noticed that the mean velocity wake had effectively decayed in 12 building heights and the turbulence wake extended to 50 heights behind a cubical obstacle on a plane surface in the wind tunnel. In general, three-dimensional wakes are smaller than two-dimensional wakes. It is reasonable to expect an obstacle having a height which is a significant fraction of the

boundary layer will create a larger relative disturbance to the boundary layer than the disturbance due to a small obstacle. Observations reported in [4] show that the mean velocity decay rate in the wake is independent of model scale size, but the magnitude of the disturbance is, in a non-dimensional sense, greater for the larger model and hence its wake persists farther downwind (Figure 3). Hunt [8] developed a theory for the wake behind a cubic block geometry and compared it with Counihan's [8] experimental results. Initial comparison gave good results but insufficient experimental data was available to test the breadth of the theory.

At present, no well-developed simple theories are available to describe the wakes behind two-dimensional obstacles. Townsend [9] investigated the effects of a change in wall boundary conditions on an equilibrium layer. In practice his analysis is only valid sufficiently far downstream of the obstacles that no new length scale is required.

Bradshaw and Wong [12] predicted that the length scale of turbulence increased rapidly above the local equilibrium value with increasing distance normal to the surface which evidently arises from the bifurcation of the mixing layer at reattachment. Thus Townsend's theory is valid for an ordinary boundary layer but not for a reattaching shear layer. Upstream from reattachment, however, the region of strong shear near the mean separation streamline is known to be reasonably described by the theory of a turbulent mixing layer [10]. However, Tani, et al. [27]

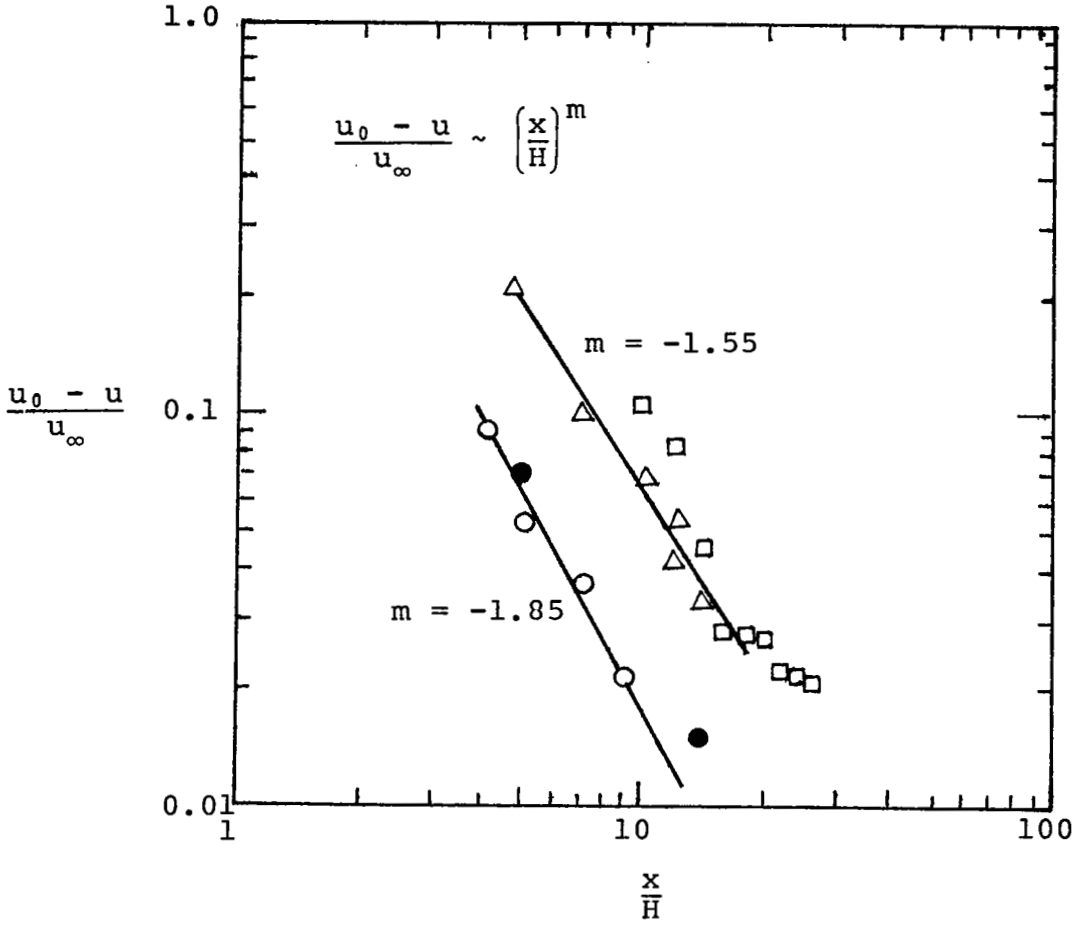

○ Model 1 (z/H = 1.08) (H/δ = 0.05)
△ Model 2 (z/H = 0.94) (H/δ = 0.107)
□ Model 3 (z/H = 0.8) (H/δ = 0.25)
● Colmer (z/H = 0.9) (H/δ = 0.017)

Figure 3. Decay of mean velocity deficit along the wake center line for values of H/δ [4].

and Mueller and Robertson [7] measured shear stress in the free shear layer much higher than that found in a plane mixing layer. The reason for higher stress is that the effective velocity difference across the shear layer is more than U_∞, the free stream velocity, due to the reversed flow in the separated region. Existing computational methods based on turbulent boundary layer concepts are not applicable to problems in which recirculation and separation occur. Since the topic of this study is directly concerned with the flow phenomena around bluff body surface obstructions to the wind and are complicated by separation and recirculation, the complete equations of motion must be considered if a realistic flow field is to be computed. Practical methods, however, for solving such equations are limited to numerical approaches which so far have assumed nonturbulent or turbulent flow based on a constant effective viscosity. More realistic turbulence models for closing the system of governing equations when Reynolds averaging has been carried out are in the development stages [21]. Considering ensemble averaged momentum equations for turbulent incompressible flow, one can have

$$\bar{u}_j \frac{\partial \bar{u}_i}{\partial x_j} = -\frac{1}{\rho} \frac{\partial \bar{P}}{\partial x_i} + \nu \frac{\partial^2 \bar{u}_i}{\partial x_j \partial x_j} - \frac{\partial}{\partial x_j} (\overline{u_i' u_j'})$$

where over-bars denote the ensemble average and superscripts "'" denote fluctuation properties. The above equation can be readily integrated if certain assumptions on the Reynolds

stress, $\rho\overline{u_i'u_j'}$, can be made to form a closed set of equations. Usually, Reynolds shear stress is expressed by the product of an eddy viscosity and a velocity gradient as follows:

$$\rho\overline{u_i'u_j'} = -\mu_t\left(\frac{\partial\bar{u}_i}{\partial x_j} + \frac{\partial\bar{u}_j}{\partial x_i}\right)$$

The eddy viscosity is a feature of turbulence so that it is a property of the flow field rather than that of the state of the fluid as is molecular viscosity. The value of eddy viscosity will thus vary from point to point in the flow, being largely determined by the structure and history of turbulence. Models for expressing the turbulent or eddy viscosity in terms of known or calculable quantities of the flow field are well described by Launder and Spalding [21]. Prandtl's mixing length model allows realistic prediction in boundary layer flows, but takes no account of the process of convection or diffusion of turbulence. The mixing length model takes

$$\mu_t = \rho\ell^2\left|\frac{\partial\bar{u}}{\partial z}\right|$$

so this means that the turbulent viscosity vanishes whenever the mean velocity gradient is zero. For the problems related to a flow downstream from a step, the mean velocity gradient is zero at the reattachment point; so if the mixing length hypothesis is adopted, the value of μ_t is also zero

there. However, the level of velocity fluctuations in the neighborhood of reattachment point has been shown to be high [21]. Generally, the local level of velocity fluctuations is determined, not only by events at the point in question but also by influences which have originated some distance upstream. In a recirculating flow, downstream happenings can also influence the value of the turbulence at any point [21]. It is important to take account of the transport characters of turbulence in the problems for which the mixing length model is not well equipped. To obtain the realistic predictions of the recirculating flow situation, the convective transport characters of turbulence have to be considered. A comparison of the performance of the different models on free shear flows [13, 20] indicates that the calculation of a length scale, ℓ, from a transport equation gives more correct predictions over a wider range of flows than is achieved with models embodying an algebraic expression for ℓ. Prandtl and Kolmogorov develop independently a turbulent model which formulates $\mu_t \sim \rho K^{1/2} \ell$, where both the turbulence kinetic energy, K, and the turbulence length scale, ℓ, are calculated from transport equations, referred to as a two-equation model. This model is used throughout this study. Gosman, et al. [11] have written a complete volume on heat and mass transfer in two-dimensional recirculating flows. Their method has been applied to turbulent flows over a bluff surface obstruction [13] and over a backward facing step [14]. The

program developed in [13] is adapted in this study to the investigation of the flow over a bluff block.

The numerical study reported in this investigation is being simultaneously supported by a field study [5] and the wind tunnel studies [4, 28,29]. The field study [5] is being conducted in the NASA Marshall Space Flight Center, Space Sciences Laboratory, Atmospheric Sciences Division Atmospheric Boundary Layer Facility (ABLF), located in Huntsville, Alabama. The tower array, located in a large open field, is schematically shown in Figure 4. There is a line of trees approximately 122 m upstream from the simulated block which are not shown. The existence of a wake from the tree line is clearly evident in the results of the field study [5]. The results from Reference [5] are summarized as follows:

1. Analysis of the mean longitudinal velocity at building level shows an overshoot at tower number 3.
2. The smoke study shows that the mean extent of the wake is 12.5 $\pm$2.3 building heights under the conditions of approximately a 16 mph wind speed at the 20m level.
3. The smoke study also indicates that the wake extends upward to a height of approximately 1.5h and 2.0h and the separation at the upstream face of the building extends forward about 0.9h.
4. The rms values of the velocity components at the 3 m level were influenced by the building but at

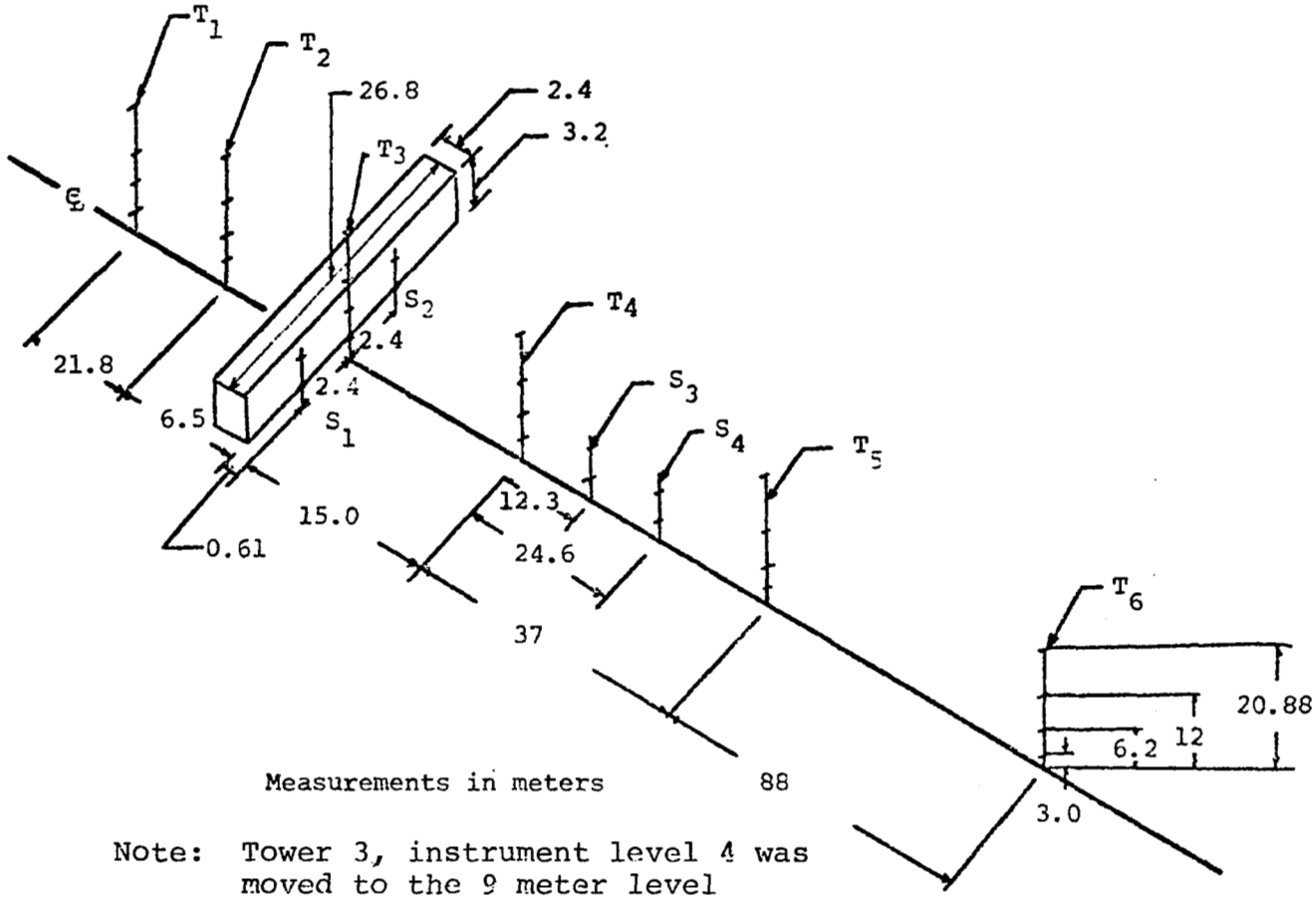

Note: Tower 3, instrument level 4 was moved to the 9 meter level

Figure 4. Tower arrangements carried out in field studies [5].

the 12 m level this influence was not apparent, indicating that the disturbulence from the building did not extend to that height.

5. The comparison of turbulence energy spectra and the ratio of velocity deviations, $\sigma_u/\sigma_v/\sigma_w$, to those of neutrally stable atmosphere over homogeneous uniform terrain reported in the literature show the influence of the tree wake to be evident.

The wind tunnel tests carried out in Reference [4] indicate the tree line in the front of the simulated block gives the flow approaching the building a higher turbulence level, Figure 5, and a higher exponent in the power-law velocity profile (from 0.25 without the trees to 0.35 with trees), Figure 6.

The power law velocity profile is described by $\frac{\bar{u}}{\bar{u}_{ref}} = \left(\frac{z}{z_{ref}}\right)^m$ which is the same as the logarithmic law if m is taken as $\frac{1}{\ell n(z_{ref}/z_o)}$.

The data from Reference [4] which did not model the trees in most of the measurements made is directly comparable to the results of this numerical study if three-dimensional effects can be neglected. These effects will be discussed and comparisons will be made in Chapter IV.

The governing equations to be solved are the Navier-Stokes equations with the Prandtl-Kolmogorov hypothesis for turbulent viscosity which requires simultaneous solution of two additional transport equations, the turbulence kinetic

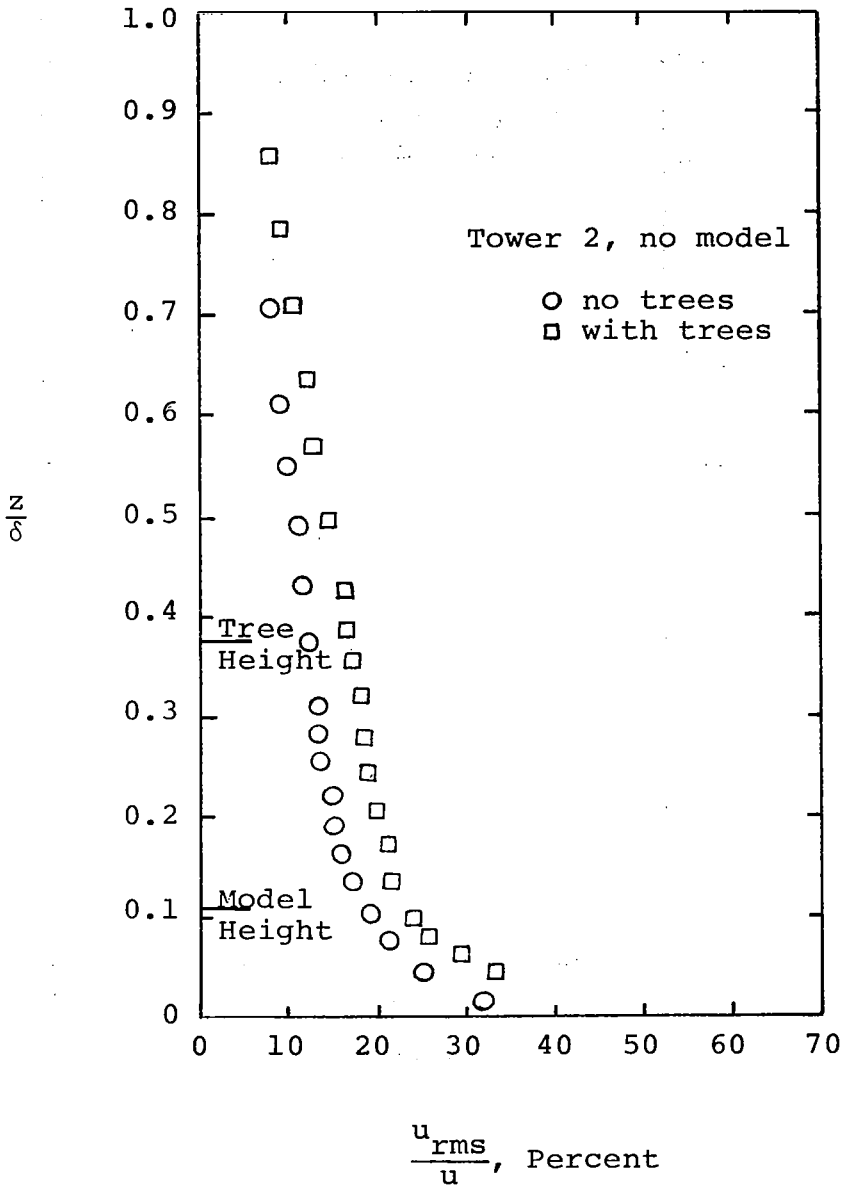

Figure 5. Vertical profile of longitudinal turbulence intensity in the approach flow [4].

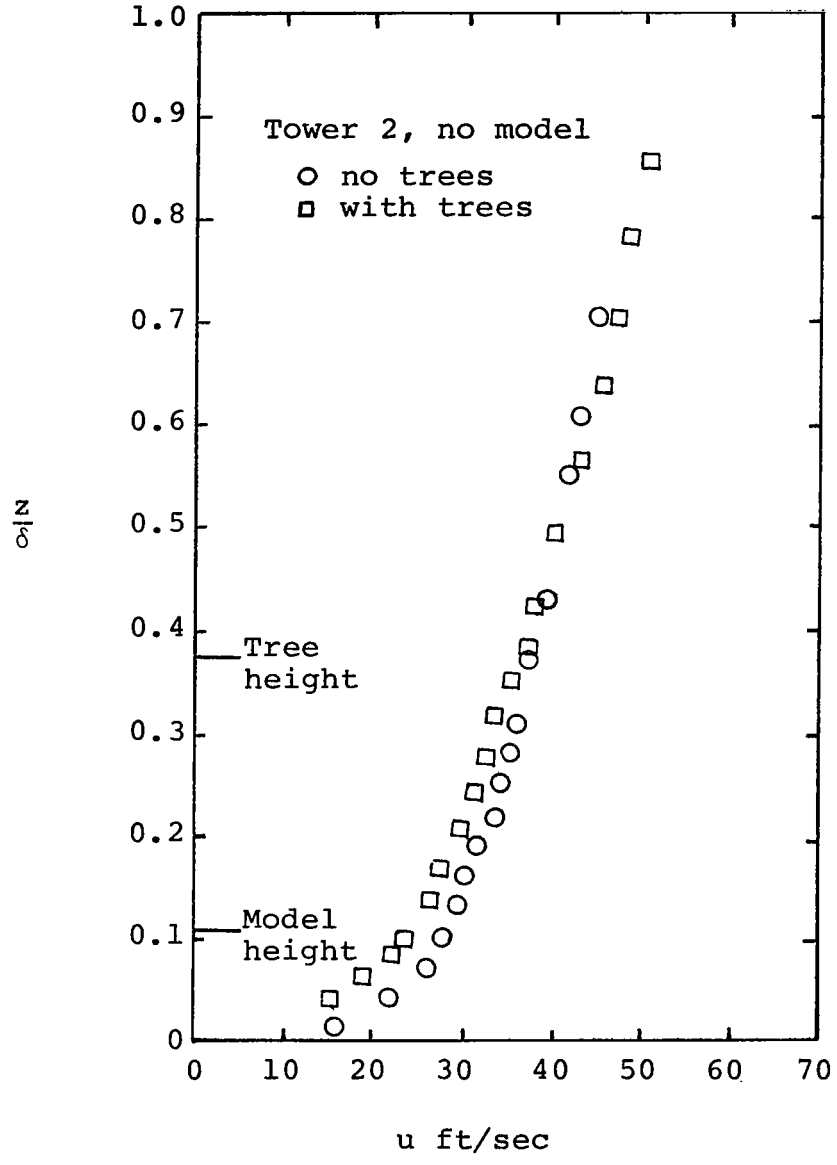

Figure 6. Vertical profile of longitudinal mean velocity in the approach flow [4].

energy and the turbulence length scale equations. The method of solution chosen is to eliminate the pressure terms involved in the equations of motion by employing the vorticity and the stream function as the dependent variable [11]. The solution is therefore obtained without any information being required about the pressure gradients.

CHAPTER II

MATHEMATIC MODEL FOR ANALYSIS OF ATMOSPHERIC FLOW OVER A TWO-DIMENSIONAL RECTANGULAR BLOCK

The complete two-dimensional Navier-Stokes equations of motion are applied to an atmospheric flow over a surface obstruction simulated by a sharp-edged rectangular block geometry as shown in Figure 1, page 3. Being a turbulent flow field, the ensemble time-average equations are used. The atmosphere is assumed to be neutrally stable and Coriolis effects induced by the rotation of the earth are considered negligible in the lower regions of the atmosphere to which the present problem is confined.

1. MEAN VELOCITY PROFILE OF APPROACHING WIND

For a neutral atmosphere, experimental evidence [15, 16] confirms the mean wind velocity in the region near the ground as being described by a logarithmic wind profile. The logarithmic wind profile is thus [17]

$$\bar{u} = \frac{u_*}{k} \ln \frac{z + z_o}{z_o} \tag{1}$$

where z_o represents the surface roughness and k is von Karman's constant. Observed wind profiles up to 150 m over

reasonably level and uniformly rough terrain under neutrally stable conditions obey this law very well [18].

2. THE TURBULENT FLUXES NEAR THE GROUND

Associated with the mean velocity gradient is a shear stress arising both from molecular or viscous momentum transport and from turbulence momentum transport. The turbulence momentum transport is generally much larger than the molecular transport. In the unstable atmospheric layer, heat transfer from the earth to the ambient air or thermal convection enhance intensity of the turbulence in the boundary. Conversely, heat transfer to the earth from the air decreases or even suppresses the turbulence in the boundary. In the neutral boundary layer, however, the effect of thermal convection is negligible and the mechanism of turbulence is solely due to the effects of shear. At a height z, small compared with the boundary layer thickness, the stress varies little from its surface value which is traditionally denoted by ρu_*^2. Reference [19] shows that:

$$-\rho\overline{u'w'} \approx \left(1 - \frac{z}{\delta}\right) \rho u_*^2 \approx \rho u_*^2, \qquad z << \delta \tag{2}$$

Equation 2 suggests that at height < 0.1δ, the shear stress is within 10% of its surface value. This has led to the concept of a "constant shear stress" layer near the earth's surface. Outdoor measurements have provided data which supports the concept of a constant-flux layer [19], Figure 7.

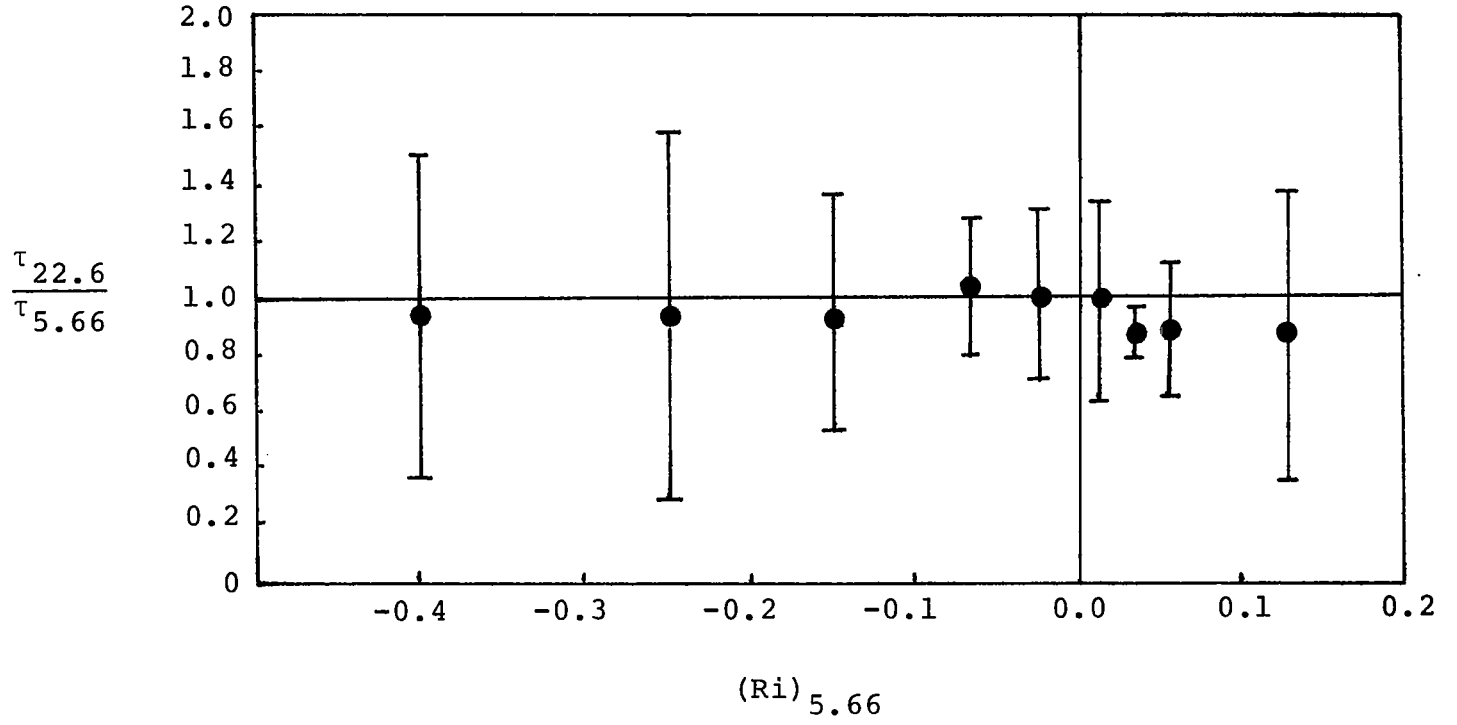

Figure 7. Ratio of stress at 22.6 and 5.66 m measured over a flat, uniform Kansas plain [19].

This stress picture is surely an idealized model since it is restricted to steady-state and horizontally homogeneous velocity conditions. However, for high wind speeds which are of primary importance to this study the concept of a neutrally, stable horizontally homogeneous and statistically steady boundary layer is meaningful.

3. GOVERNING EQUATIONS

The governing ensemble averaged turbulent flow equations for statistically steady incompressible two-dimensional flow can be written as follows:

Continuity Equation:

$$\frac{\partial \bar{u}}{\partial x} + \frac{\partial \bar{w}}{\partial z} = 0 \tag{3}$$

Momentum Equations:

(1) x direction:

$$\bar{u}\,\frac{\partial \bar{u}}{\partial x} + \bar{w}\,\frac{\partial \bar{u}}{\partial z} = -\frac{1}{\rho}\,\frac{\partial \bar{p}}{\partial x} + \frac{\partial}{\partial x}\left[\frac{\mu_{eff}}{\rho}\left(2\,\frac{\partial \bar{u}}{\partial x}\right)\right] + \frac{\partial}{\partial z}\left[\frac{\mu_{eff}}{\rho}\left(\frac{\partial \bar{u}}{\partial z} + \frac{\partial \bar{w}}{\partial x}\right)\right] \tag{4}$$

(2) z direction:

$$\bar{u}\,\frac{\partial \bar{w}}{\partial x} + \bar{w}\,\frac{\partial \bar{w}}{\partial z} = -\frac{1}{\rho}\,\frac{\partial \bar{p}}{\partial z} + \frac{\partial}{\partial z}\left[\frac{\mu_{eff}}{\rho}\left(2\,\frac{\partial \bar{w}}{\partial z}\right)\right] + \frac{\partial}{\partial x}\left[\frac{\mu_{eff}}{\rho}\left(\frac{\partial \bar{u}}{\partial z} + \frac{\partial \bar{w}}{\partial x}\right)\right] \tag{5}$$

where the overbars denote ensemble averaged quantities. The "effective viscosity," μ_{eff}, is defined by

$$\mu_{eff} = \mu + \mu_t \tag{6}$$

which is composed of molecular viscosity, μ, and of turbulent viscosity, μ_t.

For two-dimensional flow, the stream function, $\bar{\psi}$, and vorticity, $\bar{\omega}$, can be introduced by the relationships

$$\bar{u} = \frac{1}{\rho} \frac{\partial \bar{\psi}}{\partial z} \tag{7}$$

$$\bar{w} = \frac{-1}{\rho} \frac{\partial \bar{\psi}}{\partial x} \tag{8}$$

$$\bar{\omega} = \frac{\partial \bar{w}}{\partial x} - \frac{\partial \bar{u}}{\partial z} \tag{9}$$

An equation known as the stream function equation is derived from Equations 7 through 9

$$\nabla^2 \bar{\psi} = -\rho \bar{\omega} \tag{10}$$

Introducing Equations 7 through 9 into the momentum equations and then differentiating the x-momentum equation with respect to z, the z-momentum equation with respect to x, and subtracting one from the other, an equation which is generally known as the vorticity transport equation is obtained. After some arranging, the governing equation for ω becomes

$$\frac{\partial}{\partial x}\left(\bar{\omega} \frac{\partial \bar{\psi}}{\partial z}\right) - \frac{\partial}{\partial z}\left(\bar{\omega} \frac{\partial \bar{\psi}}{\partial x}\right) - \frac{\partial^2}{\partial x^2}(\mu_{eff}\, \bar{\omega}) - \frac{\partial^2}{\partial z^2}(\mu_{eff}\, \bar{\omega}) - S_\omega = 0 \tag{11}$$

where

$$S_\omega = 2 - \frac{\partial^2}{\partial x \partial z}\left[\mu_{eff}\left(\frac{\partial \bar{u}}{\partial x} - \frac{\partial \bar{w}}{\partial z}\right)\right] + \frac{\partial^2}{\partial x^2}\left[\mu_{eff}\,\frac{\partial \bar{u}}{\partial z}\right] - \frac{\partial^2}{\partial z^2}\left[\mu_{eff}\,\frac{\partial \bar{w}}{\partial x}\right] \tag{12}$$

Equation 11 reduces the two momentum equations in three variables $\bar{u}$, $\bar{w}$, $\bar{p}$, to one equation with two variables $\bar{\psi}$, $\bar{\omega}$. A turbulence closure problem arises, however, because Equation 11 contains three unknowns, $\bar{\psi}$, $\bar{\omega}$, and μ_{eff}, and only two equations (10 and 11) are available for solution. A turbulence model for μ_{eff} is therefore needed and its development is discussed in Section IV.

Both of the new governing equations (10 and 11) can be expressed in the following general elliptical equation form (Equation 11).

$$a\left[\frac{\partial}{\partial x}\left(\phi\,\frac{\partial \bar{\psi}}{\partial z}\right) - \frac{\partial}{\partial z}\left(\phi\,\frac{\partial \bar{\psi}}{\partial x}\right)\right] - \frac{\partial}{\partial x}\left[b\,\frac{\partial}{\partial x}(c\phi)\right] - \frac{\partial}{\partial z}\left[b\,\frac{\partial}{\partial z}(c\phi)\right] + d = 0 \tag{13}$$

where the coefficient functions, a, b, c, and d, corresponding to the dependent variable ϕ are given in Table I.

4. TURBULENCE MODEL

The turbulent viscosity concept provides a framework for constructing a turbulent model, but there remains the task of formulating μ_t in terms of known or calculable quantities of the mean flow.

In recirculating flows the convective transport of ℓ is expected to be large. The investigations [13, 14, 21] indicated that the two-equation model adequately accounts

TABLE 1

COEFFICIENT FUNCTIONS OF EQUATION 13

ϕ	a	b	c	d
$\overline{\psi}$	0	$1/\rho$	1	$-\overline{\omega}$
$\overline{\omega}$	1	1	μ_{eff}	$-S_{\omega}$
K	1	$\Gamma_{K,eff}$	1	$-S_{K}$
ℓ	1	$\Gamma_{\ell,eff}$	1	$-S_{\ell}$

for the convective character of turbulence in recirculating flows. The principal idea of the two-equation model is that the main local feature of a turbulent fluid can be represented by just two quantities--the kinetic energy of the fluctuating motion, K, and the length scale of the turbulence, ℓ. These two quantities are determined from appropriately determined transport equations.

Kolmogorov and Prandtl proposed a differential equation for K assuming that μ_t is dependent on the level of turbulence of the fluid and the length scale as shown in equation as reproduced here for convenience.

$$\mu_t = C_{\mu\infty} \cdot \rho K^{1/2} \ell \tag{14}$$

$C_{\mu\infty}$ is an asymptotic coefficient to be discussed later. The level of turbulence is defined as the mean kinetic energy of the velocity fluctuation, or simply the kinetic energy of turbulence.

$$K = \frac{1}{2}(\overline{u'^2 + v'^2 + w'^2}) \tag{15}$$

Combining Equations 6 and 14 and introducing a coefficient function

$$C_\mu = \left(1 + \frac{\mu}{\mu_t}\right) \cdot C_{\mu\infty} \tag{16}$$

one obtains

$$\mu_{eff} = C_\mu \rho K^{1/2} \ell \tag{17}$$

An outline of the derivation of the transport equation for K is given by Wolfshtein [22]

$$\rho\bar{u}_j \frac{\partial K}{\partial x_j} = \frac{\partial}{\partial x_j}\left(\Gamma_{K,eff} \frac{\partial K}{\partial x_j}\right) + S_K \tag{18}$$

where $\Gamma_{K,eff}$ is an exchange coefficient for the turbulence energy defined in terms of a Schmidt number based on the effective viscosity.

$$\Gamma_{K,eff} = \frac{\mu_{eff}}{\sigma_{K,eff}} \tag{19}$$

S_K, which represents "sources" and "sinks" of turbulence, is denoted as the following.

$$S_K = \mu_t\left(\frac{\partial \bar{u}_i}{\partial x_j} + \frac{\partial \bar{u}_j}{\partial x_i}\right)\frac{\partial \bar{u}_i}{\partial x_j} - C_D\rho \frac{K^{3/2}}{\ell} \tag{20}$$

C_D is a coefficient function to be determined empirically.

Rotta (1951) derived a differential equation for the length scale from the time-dependent motion. Gosman, et al. [11] reformulated the equation into the common elliptical form of their transport equation. The equation for ℓ is thus:

$$\rho\bar{u}_j \frac{\partial \ell}{\partial x_j} = \frac{\partial}{\partial x_j}\left(\Gamma_{\ell,eff} \frac{\partial \ell}{\partial x_j}\right) + S_\ell \tag{21}$$

where $\Gamma_{\ell,eff}$ is an exchange coefficient for the length scale

in terms of a Schmidt number based on the effective viscosity

$$\Gamma_{\ell,eff} = \frac{\mu_{eff}}{\sigma_{\ell,eff}} \tag{22}$$

S_ℓ is a combined source and sink term for the turbulent length scale;

$$S_\ell = -\mu_t\left(\frac{\partial \bar{u}_i}{\partial x_j} + \frac{\partial \bar{u}_j}{\partial x_i}\right)\frac{\partial \bar{u}_i}{\partial x_j} \cdot \frac{\ell}{K} \cdot C_B + \rho K^{1/2} \cdot C_S \tag{23}$$

Again C_B and C_S are coefficient functions to be determined.

Here, both the K and ℓ transport equations are taken as obeying the general form of the elliptical equation, Equation 13, and the appropriate coefficient are also given in Table I, page 24.

5. COEFFICIENT FUNCTIONS

It has been assumed that the properties of local turbulence can be characterized by the kinetic energy of the fluctuating motion, K, and the length-scale of turbulence, ℓ. From these transport properties and from the density and viscosity of the fluid, a "Reynolds number of turbulence," R_t, is defined as

$$R_t = \frac{\rho K^{1/2}\ell}{\mu} = \frac{\mu_t}{C_{\mu\infty}\mu} \tag{24}$$

Together with Equation 16, one can obtain

$$C_\mu = C_{\mu\infty} + \frac{1}{R_t}$$

It is expected that when R_t is very small, turbulence is negligible and the function tends to $1/R_t$; when R_t is very large, molecular viscosity has no significant effect and the function C_μ tends asymptotically to a constant value. An asymptotic value of C_μ for recirculating flows is determined in this report.

The function C_D is a measure of the dissipation rate per unit volume of turbulence kinetic energy. The coefficient function C_D is argued to be a function of R_t having similar behavior as that predicted for C_μ, but it cannot be presumed that the two functions have other features in common.

C_S and C_B are a measure of the positive and of the negative part, respectively, of the source and sink terms in the transport equation of the turbulence length scale. The former represents the growth of ℓ as a result of the dissipation of smaller eddies, the latter represents the reduction of ℓ from the breaking of large eddies.

C_S and C_B are taken to be functions of R_t having similar behavior as C_μ and C_D which take on a constant asymptotic value as R_t becomes large. More details of the behavior of the coefficient functions will be discussed in Chapter IV.

6. BOUNDARY CONDITIONS

It has been mentioned that the governing equations (Equations 10, 11, 18, and 21) can be expressed as a general elliptical equation having the form of Equation 13. Solutions of the elliptical equation require specifying the boundary condition on a complete contour enclosing the region in which a solution is desired. The problem of interest is thus a boundary-value problem and the prescribed boundary conditions used in this study are discussed below.

Inlet Boundary Conditions

The inlet is considered sufficiently far upstream that the flow is undisturbed by the building. Thus the inlet velocity is assumed logarithmic, Equation 1, in keeping with the wind profile of a neutral atmospheric boundary layer over flat homogeneous terrain as described in Section I. The dependent variable to be specified is the stream function which can be determined from

$$\bar{\psi} = \int_0^z \rho \bar{u}(z)\, dz$$

Assuming the no-slip condition at z = 0 and carrying out the integration gives

$$\bar{\psi} = \rho \frac{u_*}{k}\left[(z + z_0)\left(\ell n \frac{z + z_0}{z_0} - 1\right) + z_0\right] \qquad (25)$$

The vorticity, $\bar{\omega}$, is given by Equation 9, which can be

rewritten as:

$$\bar{\omega} = -\frac{1}{\rho}\left(\frac{\partial^2\bar{\psi}}{\partial x^2} + \frac{\partial^2\bar{\psi}}{\partial z^2}\right) \tag{26}$$

The vorticity at the inlet boundary is thus calculated according to Equation 26.

The boundary condition for the turbulent length scale is based on a mixing-length hypothesis which has been demonstrated as valid for boundary layer flows [21] such as is assumed to exist at the inlet boundary. In the neighborhood of the wall the mixing length is generally assumed to be linearly related to the normal distance from the surface. For a very rough surface, the mixing length hypothesis does not go to zero but approaches a size on the order of the roughness length, z_0. The following relationship is assumed:

$$\ell = k(z + z_0) \tag{27}$$

The boundary condition for the turbulence kinetic energy, K, is derived from the assumption of constant shear layer.

$$\tau_t = \tau_w = \rho u_*^2 = \text{constant} \tag{28}$$

In terms of Prandtl-Kolmogorov formula, Equation 17,

$$\tau_t = C_\mu \rho K^{1/2} \ell \left(\frac{\partial \bar{u}}{\partial z}\right) \tag{29}$$

together with Equations 1, 27, 28, and 29 gives

$$K = \left(\frac{u_*}{C_\mu}\right)^2 \tag{30}$$

Outlet Boundary Conditions

Numerous boundary conditions for $\overline{\psi}$ and $\overline{\omega}$ at the outflow boundary condition have been investigated [23]. For the flow for downstream from the surface obstacle, it is expected that

$$\frac{\partial \overline{\psi}}{\partial x} = 0 \tag{31}$$

Equation 31 implies

$$\frac{\partial^2 \overline{\psi}}{\partial x^2} = 0 \tag{32}$$

and hence,

$$\overline{\omega} = -\frac{1}{\rho} \frac{\partial^2 \overline{\psi}}{\partial z^2} \tag{33}$$

If $\overline{\psi} = 0$ along the lower boundary and if either $\overline{\psi}$ or $\frac{\partial \overline{\psi}}{\partial z}$ is fixed along the upper boundary, then the setting of $\frac{\partial^2 \overline{\psi}}{\partial z^2} = 0$ contradicts Equation 33 if $\overline{\omega} \neq 0$, or simply restates Equations 33 if $\overline{\omega} = 0$ at the upper boundary.

The gradient of vorticity in the flow direction is assumed to vanish at the outlet boundary.

$$\frac{\partial \overline{\omega}}{\partial x} = 0 \tag{34}$$

The corresponding conditions for K and ℓ at the outflow boundary are assumed to be

$$\frac{\partial K}{\partial x} = 0 \tag{35}$$

and

$$\frac{\partial \ell}{\partial x} = 0 \tag{36}$$

which describes an equilibrium boundary layer at the outlet boundary.

Upper Boundary Conditions

At the free boundary, $\bar{\psi}$ is specified by $\frac{\partial \bar{\psi}}{\partial x} = \bar{w} = 0$ and $\frac{\partial \bar{\psi}}{\partial z} = \bar{u} = u_\infty$, u_∞ is the inflow velocity at the upper boundary, i.e.,

$$u_\infty = \frac{u_*}{k} \ell n \frac{6H + z_0}{z_0}$$

which assumes the upper boundary is far enough away from the obstruction. This boundary condition implies

$$\bar{\psi} = \text{constant} \tag{37}$$

at the upper boundary.

According to Equation 26, the vorticity on the upper boundary thus becomes zero. In the free atmosphere field, however, $\bar{\omega} = 0$ may be unrealistic. A less restrictive condition for $\bar{\omega}$ is therefore assumed:

$$\frac{\partial \bar{\omega}}{\partial z} = 0 \tag{38}$$

If the upper boundary is far from the obstruction so that $\bar{w} = 0$ on the boundary, $\frac{\partial \bar{w}}{\partial x} = 0$ on the boundary and $\bar{\omega} = -\frac{\partial \bar{u}}{\partial z}$, Equation 38 implies $\frac{\partial^2 \bar{u}}{\partial z^2} = 0$. The upper boundary condition

for $\overline{\psi}$ is

$$\overline{w} = \frac{\partial \overline{\psi}}{\partial x} = 0 \tag{39}$$

The condition for K is described as a constant on the upper boundary which is expected to be neutrally stable.

$$K = \text{constant} \tag{40}$$

Similarly, ℓ is expected to be constant along the upper boundary

$$\ell = \text{constant} \tag{41}$$

Lower Boundary Conditions

The solid wall of the region of interest is a streamline along which must be constant. The conventional choice is

$$\overline{\psi} = 0 \tag{42}$$

The evaluation of wall vorticity is extremely important and can also be problematic, as it is produced by the no-slip condition at the wall and thus its specification drives the flow. By differentiating the definition of vorticity, one obtains

$$\frac{\partial \overline{\omega}}{\partial z} = \frac{\partial^2 \overline{w}}{\partial x \partial z} - \frac{\partial^2 \overline{u}}{\partial z^2} = \frac{\partial}{\partial x}\left(\frac{\partial \overline{w}}{\partial z}\right) - \frac{1}{\rho}\frac{\partial^3 \overline{\psi}}{\partial z^3} \tag{43}$$

From the continuity equation, Equation 3,

$$\frac{\partial \overline{w}}{\partial z} = -\frac{\partial \overline{u}}{\partial x} \tag{44}$$

Substituting Equation 44 into Equation 43 gives

$$\frac{\partial \overline{\omega}}{\partial z} = -\frac{1}{\rho}\frac{\partial^3 \overline{\psi}}{\partial z^3} - \frac{\partial^2 \overline{u}}{\partial x^2} \tag{45}$$

The last term is zero because of the no-slip conditions, hence,

$$\frac{\partial \overline{\omega}}{\partial z} = -\frac{1}{\rho}\frac{\partial^3 \overline{\psi}}{\partial z^3} \tag{46}$$

The treatment of the vorticity condition at the upper corners of the obstacle requires special attention and will be discussed in Chapter III.

It was assumed that K obeys Equation 30 along the wall. By differentiating Equation 1 with respect to Z

$$u_* = k(z + z_0)\frac{\partial \overline{u}}{\partial z}$$

Furthermore, at the wall, $z = 0$ and $\frac{\partial \overline{u}}{\partial z} = -\overline{\omega}$, thus

$$u_* = kz_0(-\overline{\omega})$$

substituting into Equation 30 gives

$$K_{wall} = \left(\frac{k \cdot z_0 \cdot \overline{\omega}}{C_\mu}\right)^2 \tag{47}$$

The length scale on the lower boundary was prescribed by

$$\ell = kz_0 \tag{48}$$

CHAPTER III

NUMERICAL ANALYSIS

The governing equations together with the boundary conditions and transport equations of turbulence kinetic energy and turbulence length scale constitute a closed set of nonlinear partial differential equations, given by Equations 10, 11, 18 and 21. This set of equations has been solved by utilizing and extending the numerical procedure of Gosman, et al. [11], which basically develops a set of algebraic finite-difference equations by integrating Equations 10, 11, 18 and 21 over a finite element of area. Because of the nonlinear character of the resulting finite difference equations, they are solved by an iterative, successive substitution technique. For details of the derivation of the finite difference equations, the reader is referred to References [11] and [14].

1. CONTROL VOLUME AND COORDINATE SYSTEM

The physical and numerical coordinate system for the present study is chosen such that the origin is located at the lower left corner of the block, Figure 1, page 3. The x-axis is chosen positive in the downstream direction parallel to the surface and the z-axis is perpendicular to the x-axis, chosen positive upward and aligned with the left face of the block, Figure 1. The subscripts I and J are

used to index the x-direction and z-direction respectively in the numerical calculation procedure. In the iteration process the field was swept from the upper boundary to the lower boundary beginning at the inlet boundary and proceeding in the increasing I-direction.

The distribution of the grid points is shown in Figure 8. As indicated, a variable mesh was used which gradually decreased in size near the wall and in the vicinity of the step.

2. BOUNDARY CONDITIONS TREATED IN THE NUMERICAL SOLUTION

The boundary conditions have already been established in Chapter II. The transformations of these into the finite difference form used in the numerical procedure are described next.

Inlet Flow:

Equations 25, 27 and 30 are directly applicable in their original form. The vorticity at the inlet boundary is treated by the assumption that $\frac{\partial^2 \bar{w}}{\partial x^2} = 0$. Setting

$$\left.\frac{\partial \bar{w}}{\partial x}\right|_{1,J} = \left.\frac{\partial \bar{w}}{\partial x}\right|_{2,J} = -\frac{1}{\rho}\left.\frac{\partial^2 \bar{\psi}}{\partial x^2}\right|_{2,J} \tag{49}$$

Together with Equations 1, 9 and 26

$$\bar{\omega} = -\frac{1}{\rho}\left.\frac{\partial^2 \bar{\psi}}{\partial x^2}\right|_{2,J} - \frac{u_*}{k}\frac{1}{z + z_0} \tag{50}$$

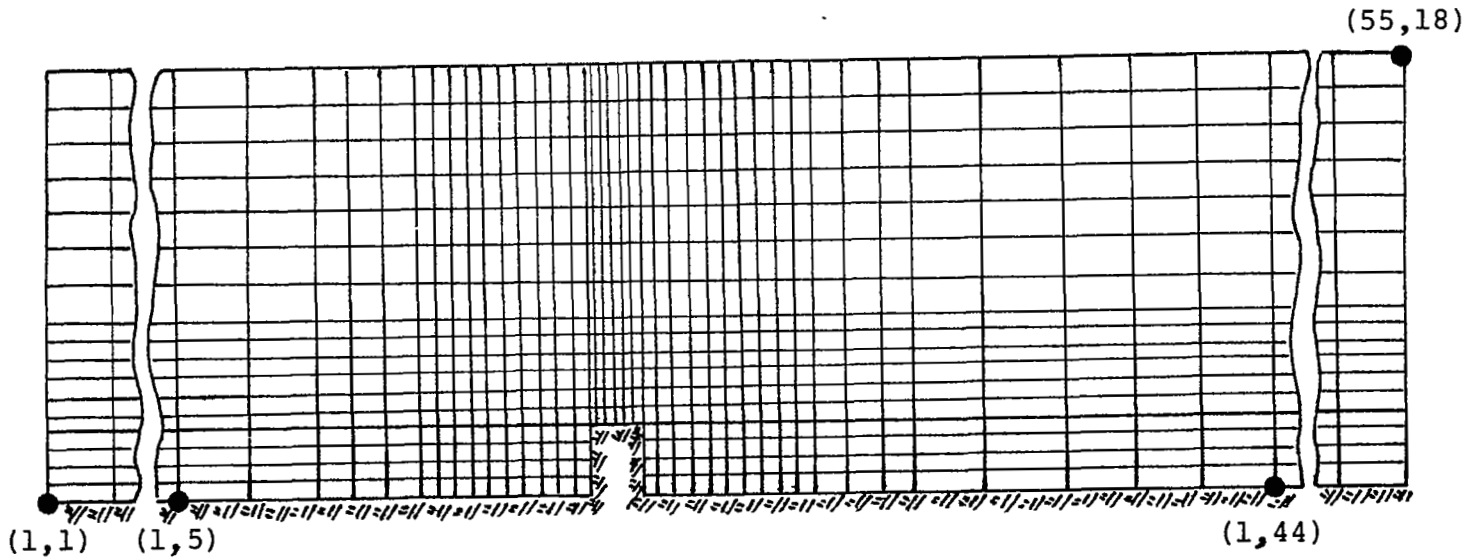

Figure 8. Grid distribution.

where

$$-\frac{1}{\rho}\left.\frac{\partial^2\overline{\psi}}{\partial x^2}\right|_{2,J} = -\frac{1}{\rho}\frac{\overline{\psi}_{3,J} + \overline{\psi}_{1,J} - 2\overline{\psi}_{2,J}}{(\Delta x)^2}$$

Outlet Flow:

Equation 32 is used for the outlet boundary conditions far downstream from the block. It is rewritten

$$\left.\frac{\partial^2\overline{\psi}}{\partial x^2}\right|_{IN,J} = \left.\frac{\partial^2\overline{\psi}}{\partial x^2}\right|_{IN-1,J} = \frac{\overline{\psi}_{IN,J} - 2\psi_{IN-1,J} + \psi_{IN-2,J}}{(\Delta x)^2} = 0$$

where x is uniform at the outlet boundary, which yields

$$\overline{\psi}_{IN,J} = 2\overline{\psi}_{IN-1,J} - \overline{\psi}_{IN-2,J} \tag{51}$$

The finite difference forms of the vorticity, the turbulence kinetic energy and the turbulence length scale are written in the following:

$$\begin{aligned}\overline{\omega}_{IN,J} &= \overline{\omega}_{IN-1,J}\\ K_{IN,J} &= K_{IN-1,J}\\ \ell_{IN,J} &= \ell_{IN-1,J}\end{aligned} \tag{52}$$

Upper Boundary:

The partial differential form of Equations 38, 39, 40 and 41 are transferred as

$$\begin{aligned}\overline{\omega}_{I,JN} &= \overline{\omega}_{I,JN-1}\\ \overline{\psi}_{I,JN} &= \overline{\psi}_{1,JN}\end{aligned}$$

$$K_{I,JN} = K_{1,JN}$$

$$\ell_{I,JN} = \ell_{1,JN} \tag{53}$$

Lower Boundary:

The vorticity at the lower boundary is developed from a Taylor-series expansion of the stream function around a near wall point (NP) located a distance n from the wall. In terms of the wall point (P), $\bar{\psi}_{NP}$ becomes:

$$\bar{\psi}_{NP} = \bar{\psi}_P + \left.\frac{\partial\bar{\psi}}{\partial n}\right|_P \Delta n + \frac{1}{2}\left.\frac{\partial^2\bar{\psi}}{\partial n^2}\right|_P (\Delta n)^2 + \frac{1}{6}\left.\frac{\partial^3\bar{\psi}}{\partial n^3}\right|_P (\Delta n)^3 + \text{H.O.T.} \tag{54}$$

By the no-slip condition, $\frac{\partial\bar{\psi}}{\partial n} = 0$ and $\frac{\partial^2\bar{\psi}}{\partial n^2} = -\rho\bar{\omega}$, and together with Equation 46, Equation 54 becomes

$$\bar{\omega}_P = -\frac{2(\bar{\psi}_{NP} - \bar{\psi}_P)}{(\Delta n)^2 \cdot \rho} - \left(\frac{\partial\bar{\omega}}{\partial n}\right)_P \frac{\Delta n}{3} \tag{55}$$

The vorticity gradient at the wall was approximated by

$$\left(\frac{\partial\bar{\omega}}{\partial n}\right)_P = \frac{\bar{\omega}_{NP} - \bar{\omega}_P}{\Delta n} \tag{56}$$

which yields upon substitution into Equation 54

$$\bar{\omega}_P = -\frac{3(\bar{\psi}_{NP} - \bar{\psi}_P)}{(\Delta n)^2 \cdot \rho} - \frac{1}{2}\bar{\omega}_{NP} \tag{57}$$

A special treatment of the vorticity at the upper corners of the rectangular block is discussed in [13]. The back corner is treated similarly as shown below. Based on

the idea that separation occurs tangentially to the upstream wall, one can apply Equation 56 to the upstream wall of the block and obtain the vorticity at the upper front corner, ω_C, (see Figure 9) as:

$$\bar{\omega}_C = -\frac{3\bar{\psi}_W}{\rho(\Delta x)^2} - \frac{1}{2}\bar{\omega}_W \tag{58}$$

and the vorticity at the upper rear corner, $\bar{\omega}_D$, as:

$$\bar{\omega}_D = -\frac{3\bar{\psi}_N}{\rho(\Delta z)^2} - \frac{1}{2}\bar{\omega}_N \tag{59}$$

3. SELECTION OF THE COEFFICIENT FUNCTIONS

Based on the discussion of Section 5, Chapter II, the coefficient functions, C_μ, C_D, C_B, C_S, are all expected to take on constant asymptotic values as R_t becomes very large, say $C_{\mu\infty}$, $C_{D\infty}$, $C_{B\infty}$ and $C_{S\infty}$, respectively. Research using the two-equation modeling of turbulence has not resolved the exact values of those constants which are assigned radically different values by different researchers depending on the flow situation being analyzed.

Wolfshtein [22], modeling a jet impinging normally on a wall, found values of $C_{\mu\infty} = 0.22$, $C_{D\infty} = 0.416$ and $\sigma_{K,eff} = 1.53$. Rodi and Spalding [24], using production of turbulence kinetic energy and length scale, $K\ell$, as a dependent variable instead of ℓ ($K - K\ell$ model), obtained $C_{D\infty} = 0.09$ for free shear flows while $\sigma_{K,eff}$ was taken as 2.0. Ng and Spalding [25] compared boundary layer flows near smooth

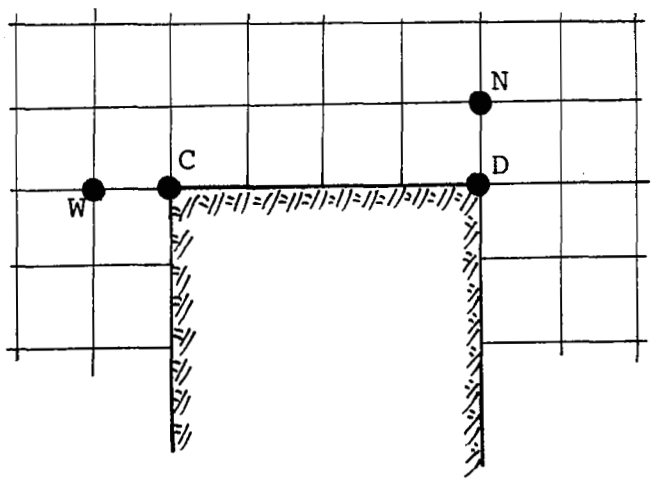

$$\bar{\omega}_C = -\frac{3\bar{\psi}_W}{(\Delta x)^2 \cdot \rho} - \frac{1}{2}\bar{\omega}_W$$

$$\bar{\omega}_D = -\frac{3\bar{\psi}_N}{(\Delta z)^2 \cdot \rho} - \frac{1}{2}\bar{\omega}_N$$

Figure 9. Boundary conditions for vorticities at upper corners of block.

wall predicted with the (K - Kℓ model) against experimental results for homogeneous shear flows in local equilibrium and obtained $C_{D\infty} = 0.1$, $C_{\mu\infty} = 1.0$ with $\sigma_{K,eff} = 1.0$. Launder, et al. [20], employing turbulence kinetic energy dissipation rate, $\varepsilon = K^{3/2}/\ell$, as the dependent variable instead of ℓ found $C_{\mu\infty} = 0.09$ and $\sigma_{K,eff} = 1.0$ for free turbulent shear flows. In view of the fact that no consistent values of the coefficient have been reported for use in the present study and that experimental data is scarce, it was necessary to develop some understanding of the coefficient functions. This is discussed in Chapter IV. Throughout this study $\sigma_{K,eff}$ and $\sigma_{\ell,eff}$ are simply assumed to be unity which is consistent with most turbulent flow analysis.

4. ACCURACY, CONVERGENCE AND ECONOMY

In carrying out the numerical solution, a balance is required between the convergence and accuracy of the results and the amount of computing time necessary to meet these conditions. The accuracy and economy of the solution procedure are opposed to one another, i.e., the finer the grid size, the more computing time required but the better the accuracy or truncation error.

A very fine grid size is required, especially near the wall, where steep gradients occur. To assure accuracy, Wolfshtein [22] found by comparing the exact and the finite-difference solutions for the cases of Couette flow, impinging flow and uniform velocity flow that a finer grid away from

the wall did not improve the accuracy of the vorticity solution, but that the stream function was sensitive to the grid size. In general, coarser grids were used at a reasonable distance away from the walls to cut down the computing time; however, one of the most important factors affecting the convergence is the grid spacing.

Gosman, et al. [11], suggested that the ratio of the consecutive intervals between the nodes normal to the wall should be as close to unity as possible, especially near the wall but in no case should they be less than 1.5. This suggestion was adopted in References [13] and [14], and is also adopted in this study. It was found, in keeping with Gosman, et al. [11], that convergence was impaired when a grid having a ratio greater than 2 between the node intervals was used, especially in the z-direction [14]. Maintaining a uniform grid spacing near the wall assured convergence as reported in Reference [13] and as experienced in this study.

A commonly employed remedy against divergence of the iteration process is known as under-relaxation. For the present problem there was no need for under-relaxation; however, in fact, the stream function, related to the vorticity by a Poisson type equation (Equation 10), was over-relaxed and the convergence of the solution accelerated.

5. TERMINATION OF COMPUTATION

The computation was assumed to have converged to a sufficiently exact solution of the difference of the

dependent variable ϕ at all points between successive iterations became small, i.e.,

$$\left| \frac{\phi_P^N - \phi_P^{N-1}}{\phi_P^N} \right|_{max} \leq 0.05$$

The superscript N denotes the nth iteration. ϕ_P was chosen in the denominator as a scaling factor in order to assure relatively good convergence in all areas.

CHAPTER IV

RESULTS AND DISCUSSIONS

1. INVESTIGATION OF COEFFICIENT CONSTANTS

The influence of the variation of the constants on the flow field is studied in the present investigation. Taking the ratio of the production term to the dissipation term in Equations 20 and 23, one obtains

$$\frac{K_C}{K_D} = \left(\frac{C_{\mu\infty}}{C_{D\infty}}\right)\left(\frac{\ell^2}{K}\left(\frac{\partial \bar{u}_i}{\partial x_j} + \frac{\partial \bar{u}_j}{\partial x_i}\right)\frac{\partial \bar{u}_i}{\partial x_j}\right) \tag{60}$$

$$\frac{\ell_C}{\ell_D} = \left(\frac{C_{S\infty}}{C_{\mu\infty}C_{B\infty}}\right)\left(\frac{K}{\ell^2}\,\frac{1}{\left(\frac{\partial \bar{u}_i}{\partial x_j} + \frac{\partial \bar{u}_j}{\partial x_i}\right)\frac{\partial \bar{u}_i}{\partial x_j}}\right) \tag{61}$$

where subscripts "C" and "D" denote the production term and dissipation term in Equations 20 and 23, respectively. $C_{\mu\infty}$, $C_{D\infty}$, $C_{B\infty}$ and $C_{S\infty}$ are discussed in Section 5 in Chapter II, and in Section 3 in Chapter III. Thus

$$\frac{K_C}{K_D} \cdot \frac{\ell_C}{\ell_D} = \frac{C_{S\infty}}{C_{D\infty}C_{B\infty}} \tag{62}$$

In view of the fact that the last terms of Equations 60 and 61 are always positive and the assumption that the influence of those last terms on the $\frac{K_C}{K_D}$ and $\frac{\ell_C}{\ell_D}$ ratios are always in the same order, it is expected that these ratios should lead

to some understanding of the turbulent levels. For example:

1. Decreasing the ratio $\frac{C_{\mu\infty}}{C_{D\infty}}$ decreases the production of turbulent kinetic energy either through less production or faster dissipation.
2. Decreasing the ratio $\frac{C_{S\infty}}{C_{\mu\infty}C_{B\infty}}$ with $C_{\mu\infty}$ constant decreases the growth of the length scale.

The individual behavior of the coefficient constants can be described as listed below:

a. Decreasing $C_{\mu\infty}$ decreases turbulent kinetic energy production and also increases the growth rate of the turbulent length scale.

b. Increasing $C_{D\infty}$ reduces the level of turbulent kinetic energy by increasing the rate at which it is dissipated.

c. Decreasing $C_{S\infty}$ or increasing $C_{B\infty}$ decreases the rate of growth of the turbulent length scale.

The influence of $C_{\mu\infty}$ on the turbulent level is illustrated from Equation 30. The inlet condition of turbulence kinetic energy is strongly dependent on C_{μ} and thus the variation of $C_{\mu\infty}$ will influence the turbulence kinetic energy over the entire flow field. This is reasonable in that the turbulence level in the incident flow should influence the flow in the region of interest. The smaller $C_{\mu\infty}$ value will cause larger turbulence kinetic energy in the flow field. This fact appears opposite to the prediction "a," above; however, it suggests that the higher the incident turbulence the lower the production rate which is not

implausible. The behavior of $C_{\mu\infty}$ still requires further investigation.

Frost and Harper [26] point out that for the atmospheric boundary layer it has been experimentally determined that

$$\sigma_u = 2.5\ u_*$$
$$\sigma_v = 1.9\ u_*$$
$$\sigma_w = 1.3\ u_*$$

for a neutral atmosphere, where

$$\sigma_u = (\overline{u'^2})^{1/2}$$
$$\sigma_v = (\overline{v'^2})^{1/2}$$
$$\sigma_w = (\overline{w'^2})^{1/2}$$

These relationships together with Equation 15 give

$$K = 5.78\ u_*^2 \tag{63}$$

Considering the inlet boundary condition for turbulent kinetic energy given by Equation 30, one obtains

$$C_{\mu\infty} = 0.416 \tag{64}$$

for the neutrally stable atmosphere. This value of $C_{\mu\infty}$ is adopted throughout the remainder of this investigation. Two cases were chosen to investigate the influence of the coefficient constants. They are:

Case I:

$C_{\mu\infty} = 0.416$ $\qquad$ $C_{S\infty} = 1.0$

$C_{D\infty} = 1.0$ $\qquad$ $C_{B\infty} = 1.0$

Case II:

$C_{\mu\infty} = 0.416$ $\qquad$ $C_{S\infty} = 0.60$

$C_{D\infty} = 0.43$ $\qquad$ $C_{B\infty} = 1.40$

The behavior of the ratios, $\frac{C_{\mu\infty}}{C_{D\infty}}$ and $\frac{C_{S\infty}}{C_{\mu\infty}C_{B\infty}}$, are considered rather than the individual variation of the coefficients. Figure 10 indicates the turbulent kinetic energy of Case II is larger than that of Case I at the corresponding position in the flow field. This is expected because

$$\left(\frac{C_{\mu\infty}}{C_{D\infty}}\right)_{II} > \left(\frac{C_{\mu\infty}}{C_{D\infty}}\right)_{I}$$

meaning the ratio of production to dissipation is greater for Case II than Case I. Figure 11 shows the turbulent scale for Case I is larger than that of Case II at the corresponding point in the flow field. This effect is caused by the fact

$$\left(\frac{C_{S\infty}}{C_{\mu\infty}C_{B\infty}}\right)_{I} > \left(\frac{C_{S\infty}}{C_{\mu\infty}C_{B\infty}}\right)_{II}$$

It is observed that the qualitative behavior of the results shown in Figures 10 and 11 are very similar despite

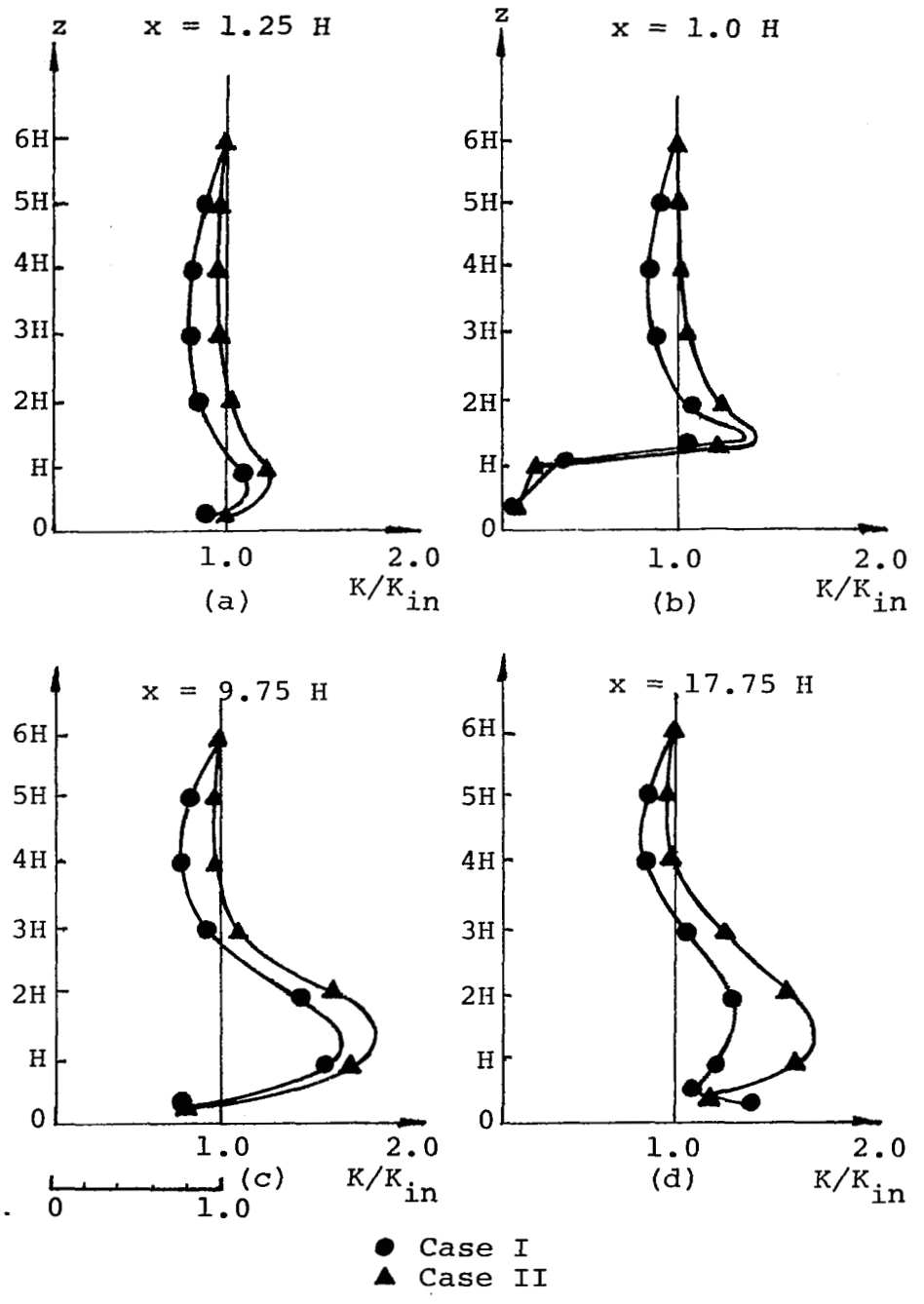

Figure 10. Comparison of the turbulence kinetic energy for different constants' ratio.

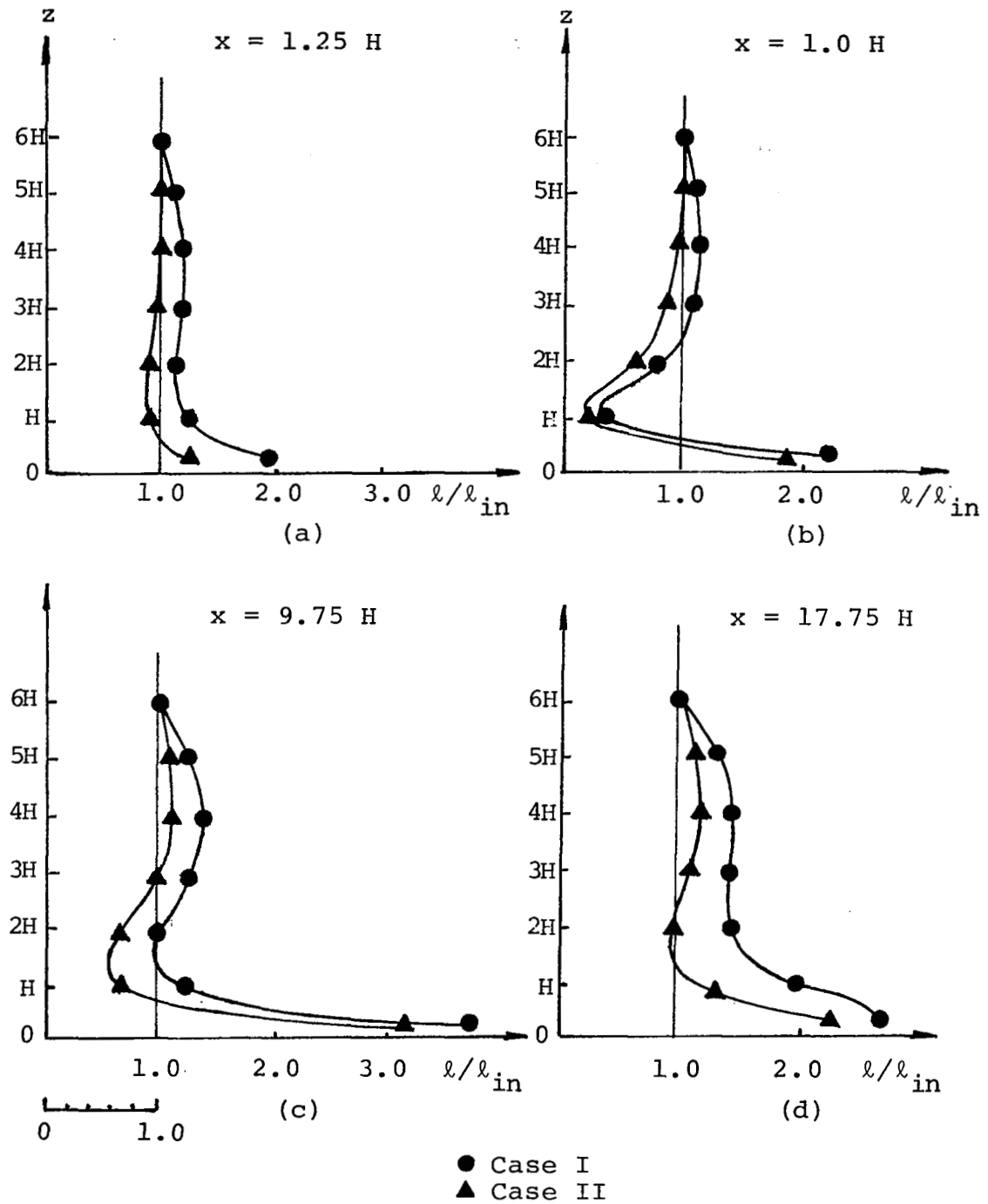

Figure 11. Comparison of the turbulence length scale for different coefficient constants' ratio.

the choice of the coefficient constants but that the quantitative results depend on the selection of these coefficient constants.

To establish some physical explanation of the ratio $\frac{C_{S\infty}}{C_{\mu\infty}C_{B\infty}}$ one can argue that the growth of the turbulent length scale is a result of dissipation of energy which creates the biggest fatality rate for small eddies. Thus when dissipation exceeds production the length scale, which is taken to represent some effective mean of the distribution of length scales, will increase with the depletion of the smaller eddies. The reduction in the length scale, in turn, may be thought of as being caused by the tendency of shear stress to rupture the large eddies. Therefore, when the production of turbulence kinetic energy exceeds dissipations the length scale will decrease and when the dissipation exceeds production the length scale will grow. Hence one might suspect

$$\frac{\ell_C}{\ell_D} \propto \frac{K_D}{K_C} \tag{65}$$

and we assume here the relationships

$$\frac{K_C}{K_D} \cdot \frac{\ell_C}{\ell_D} = \frac{C_{S\infty}}{C_{D\infty}C_{B\infty}} = 1.0 \tag{66}$$

This assumption is at least valid for quantitative study. The relationships of coefficient constants are generally derived under the consideration of an equilibrium boundary layer, Appendix A, but this approach is not suitable in the

more complex flow problem presented herein. Due to the experiences with the present computer code reported in References [13, 14], the program is known to work well when all the coefficient constants are chosen to be unity. Taking cognizance of these experiences and considering Equation 66, the following values are chosen for the qualitative studies.

Case III:

$C_{\mu\infty} = 0.416$ $\qquad$ $C_{S\infty} = 0.6$

$C_{D\infty} = 0.416$ $\qquad$ $C_{B\infty} = 1.44$

The results of a qualitative study with these values and for $u_* = 36.63$ cm/sec and $z_0 = 0.7$ cm are reported in the next section.

2. VELOCITY DISTRIBUTION

The velocity distribution of the flow around a bluff obstruction is one of the most interesting topics in current numerical fluid mechanics research. Figure 12 shows the computed velocity profiles at selected X stations. In the region close to the wall, the flow is decelerated as it approaches the obstruction and is accelerated as it passes over the obstruction. A recirculating flow region which extends approximately 11 step heights downstream is created behind the obstruction. In the region above the recirculation zone, the flow is accelerated because of the displacement of the flow. The flow reattaches near X = 12.25 H and

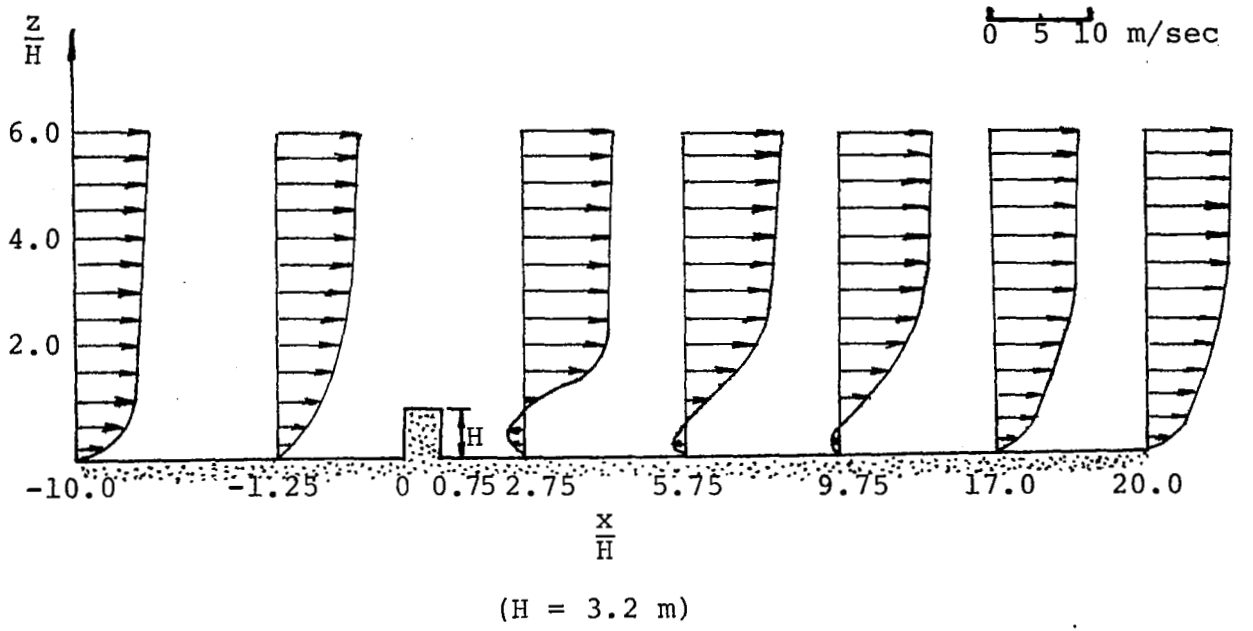

Figure 12. Velocity profiles around an obstruction on the surface.

the logarithmic boundary layer begins to reestablish downstream. Figure 13, which is a plot of the local velocity profiles nondimensionalized with the upstream value clearly demonstrates the phenomena described above. The results in Figure 13 clearly support the often reported observation [12] that the flow tends to equilibrium at a much slower rate than the rate at which the disturbance process takes place. Figure 12 indicates that at 20 step heights behind the obstruction the flow has not redeveloped to the initial state. This is supported by Reference [5] which reported that 44 step heights were required for the flow to return to equilibrium.

3. TURBULENCE KINETIC ENERGY

Figure 14 gives some computed information about the tendency of turbulent kinetic energy in the flow field. In this study, ψ, ω, K and ℓ are chosen as the four dependent variables. The behavior of any one of these dependent variables influences all of the others. Comparing Figures 14 and 13, one concludes that the deceleration of flow in the flow direction tends to increase the turbulent kinetic energy and that the acceleration of the flow in the downwind direction reduces the local turbulent kinetic energy. The extremely small value of the turbulent kinetic energy found below z = H at 0.25 H behind the obstruction is believed to be caused by the rear face of the obstruction restricting the fluctuation in that region. Turbulent kinetic energy

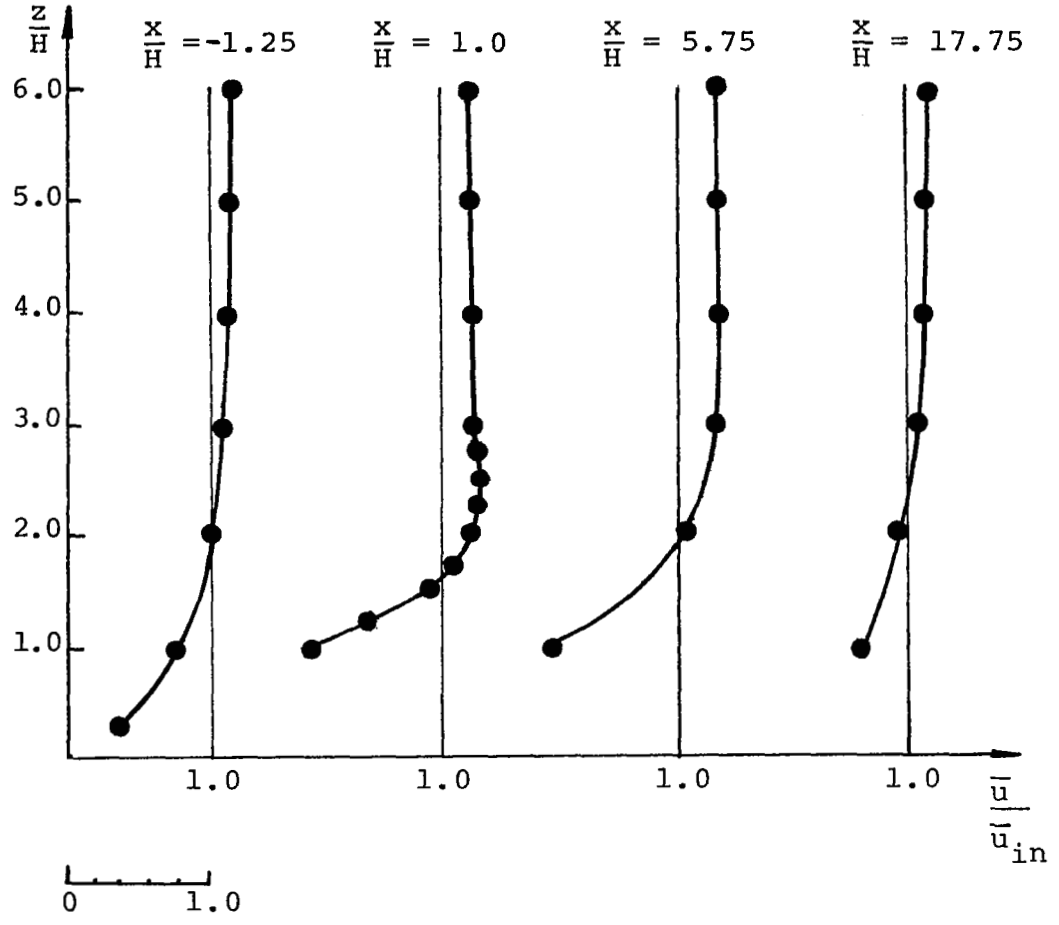

Figure 13. The ratio of local mean velocity in direction x to that of the inlet condition at the same altitude.

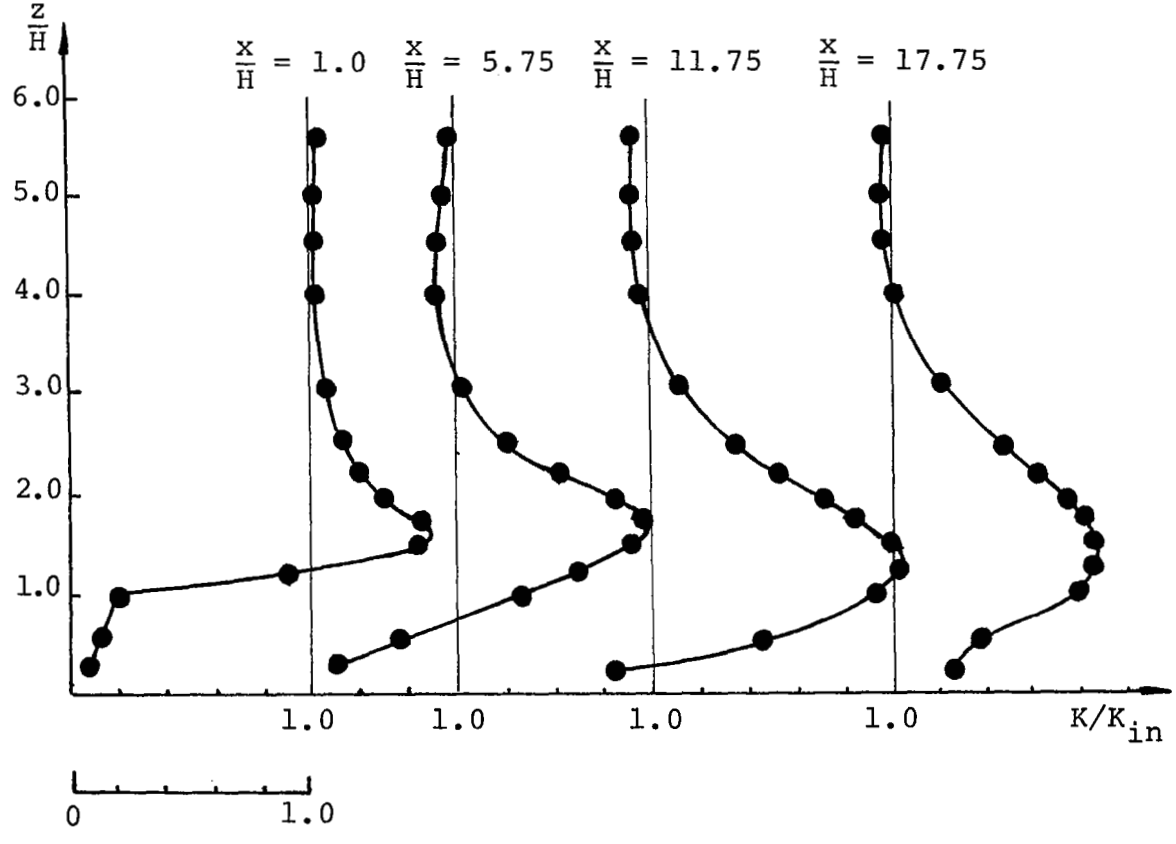

Figure 14. The ratio of local turbulence kinetic energy to that of inlet condition at the same altitude.

near a solid surface has typically low values because the random motion of fluid particles is restricted.

One can trace the shear layer separating from the front face of the block and diffusing outward as it moves downstream. This shear layer is highly turbulent as the computation clearly portrays. One can also well observe the diffusive action of the turbulence kinetic energy in the shear layer originating from the corner of the block. Figure 14 shows that the turbulent kinetic energy reaches its peak value over the reattachment point and then begins to decrease and to tend to a stable state downstream. Turbulent kinetic energy decrease in the flow direction behind the reattachment point is almost the same as that of turbulent kinetic energy increase in front of the reattachment point. The turbulence intensity is still considerably in excess of the initial value at 17 step heights downstream.

4. TURBULENCE LENGTH SCALE

The turbulent length scale employed herein is the integral of the two point velocity correlation in the flow direction. This is called the integral length scale and is considered a measure of the largest eddy size. The turbulent scale growth was suggested as representing the effect of preferential dissipation of smaller eddies by turbulence kinetic energy dissipation. Considering the ratio of turbulence length scale to the initial value, Figure 15, and that of velocity to the inlet value, Figure 13, page 55, one

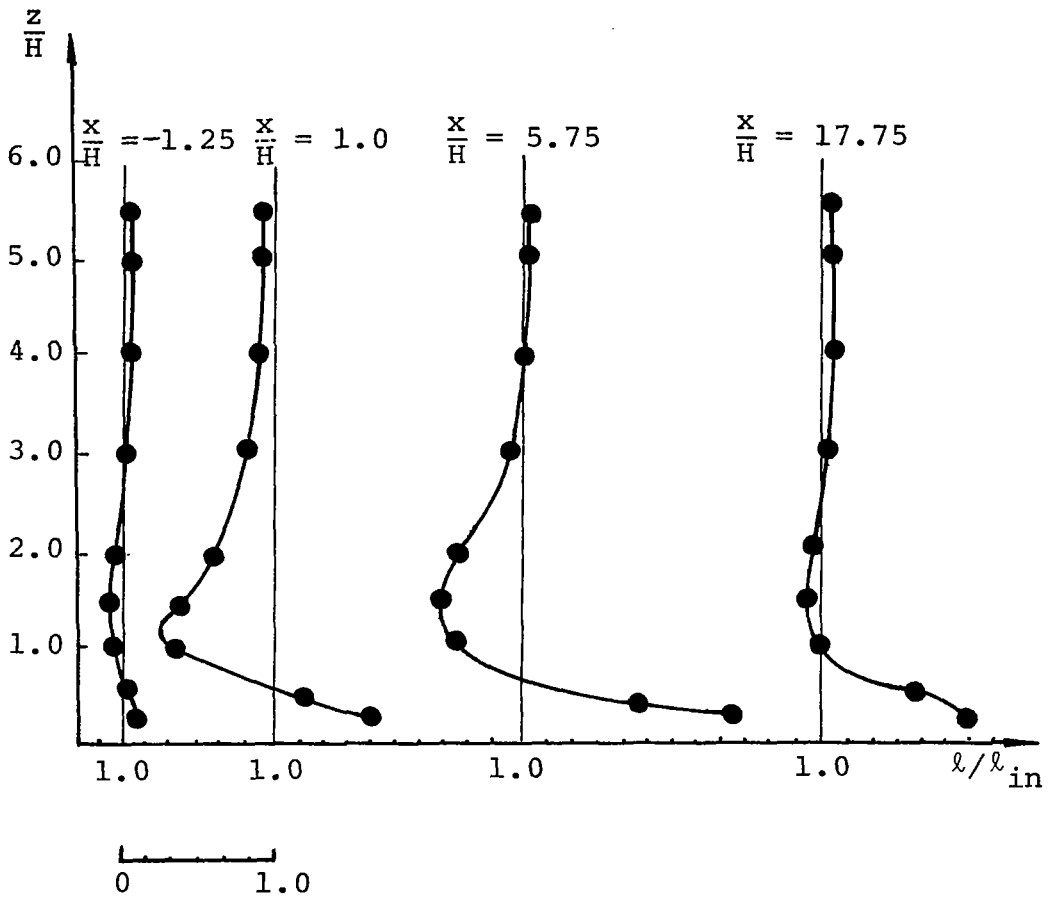

Figure 15. The ratio of local turbulence length scale to that of the inlet condition at the same altitude.

can observe that the acceleration in the flow direction always shrinks the eddy length. The effect of deceleration gives the opposite effect.

The large length scale near the lower corners of the obstruction may be explained in terms of the two vortices near the front and rear lower corners, respectively. Further discussion of these vortices are given in the next section.

5. VORTICITY AND STREAMLINE PATTERNS

Both computed vorticity contours, Figure 16, and streamline patterns, Figure 17, indicate that a small downwash zone occurs near the front lower corner and a large recirculation zone occurs behind the obstruction. For theoretical analysis the boundaries of both zones are chosen as the streamline, $\overline{\psi} = 0$. The zero streamlines divide the mixing region, which comprises the original and part of the new shear layer, and the outer flow from the downwash zone and recirculation zone where the fluid recirculates as a large eddy.

6. COMPARISON OF COMPUTED RESULTS WITH EXPERIMENTAL DATA

Two data sets obtained from the field tests (see Chapter I), data sets #8505 and #8512 [5] are chosen for comparison with the calculated results. Figure 18 shows non-dimensional velocity profiles, the local velocity divided by

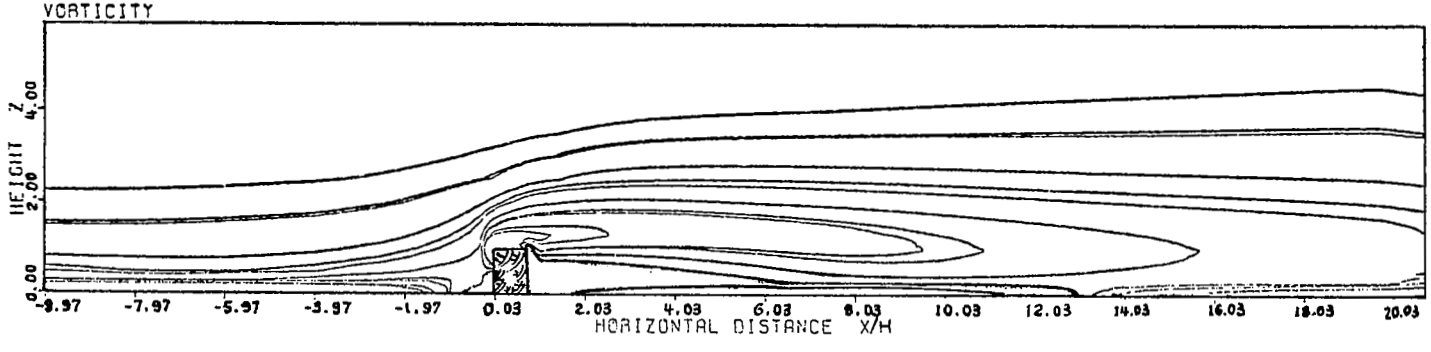

Figure 16. Vorticity contour.

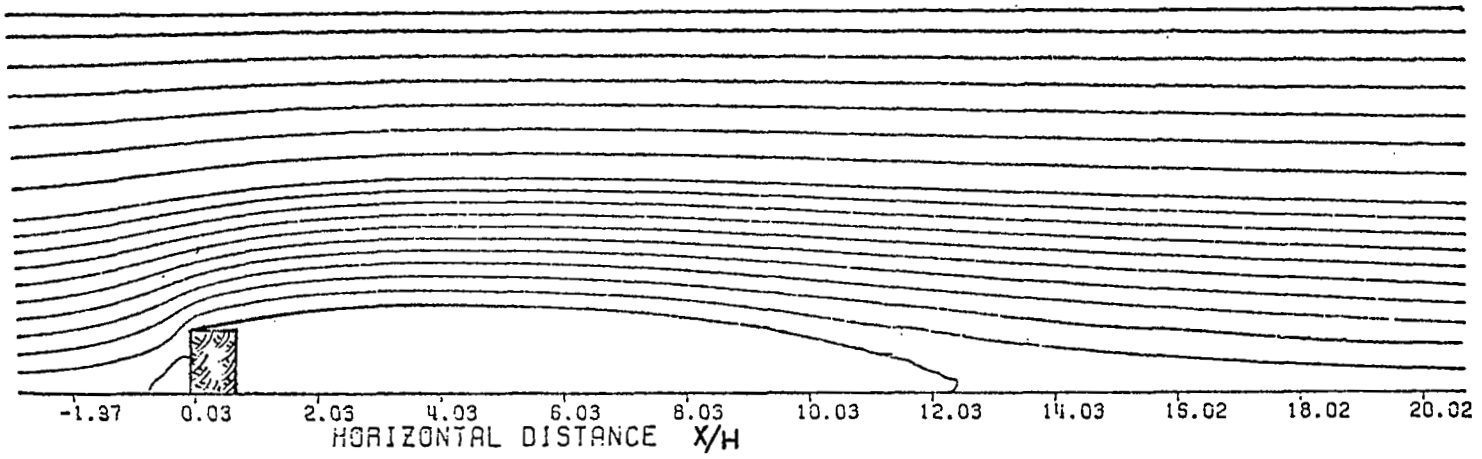

Figure 17. Streamline patterns.

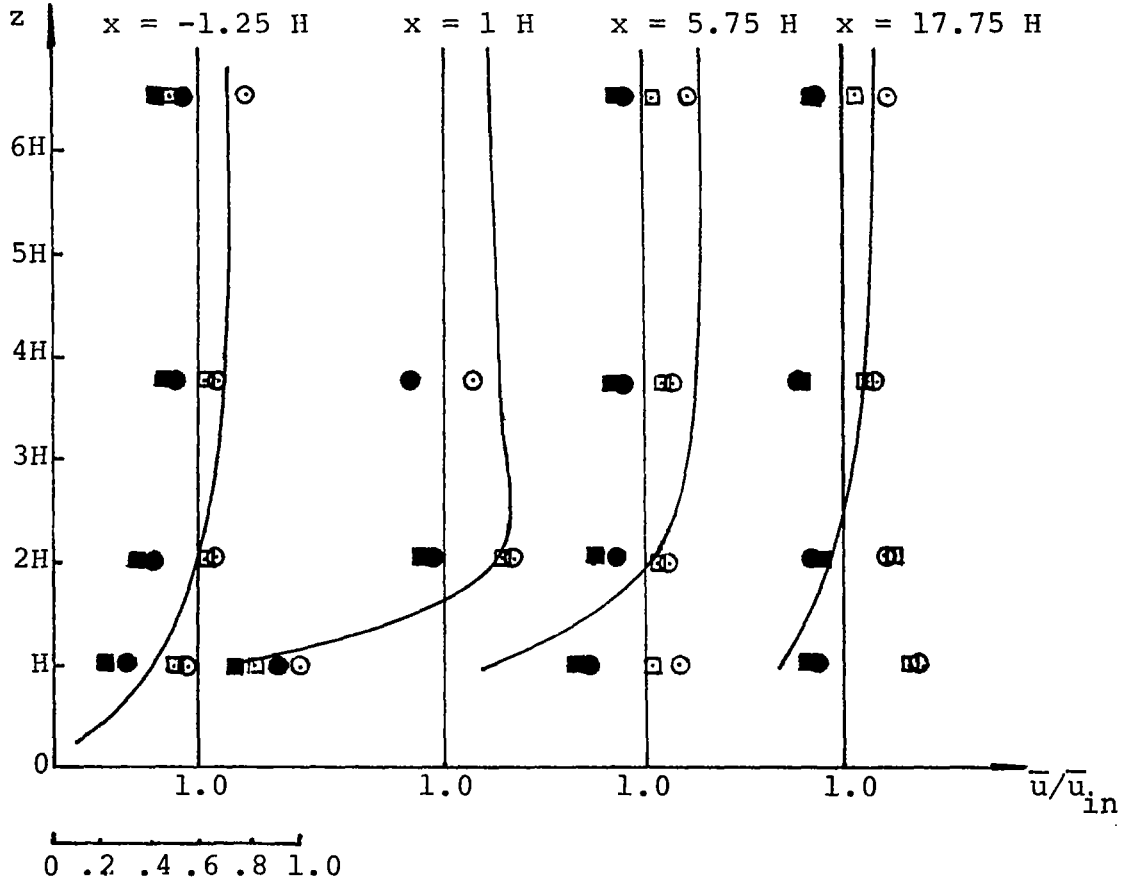

Figure 18. Comparison of the ratio $\bar{u}/\bar{u}_{in}$.

the inlet velocity at the same altitude, and Figure 19 shows nondimensional turbulence kinetic energy profiles, the local value divided by the inlet magnitude at the same altitude at several x stations down the array. Observing Figure 18, one notes that the computed results show reasonable agreement at the upstream stations but depart appreciably at the downstream locations. Figure 18 indicates the experimental velocity deficit, $u_{in} - u$, decays by 5 block heights downwind from the block. This value is far smaller than that obtained in the wind tunnel studies (see Chapter I) and of that found in Reference [5] which conducted smoke tests and showed that reattachment occurs at 12 H. The computed results indicate that the velocity defect decays in the same manner as the observation of the wind tunnel tests [28]. The details of this comparison will be performed later.

At the location x = 17.75 H, the nondimensional velocity has an unexpected shift from the expected value of unity at the lower levels. In the field tests, there is a small hill in front of Tower #5 which is located at 16.5 H behind the block. This hill is expected to create an acceleration due to mass conservation and the velocity u will thus exceed the upstream value causing $\frac{u}{u_{in}}$ to be greater than unity. If one assumes the measurement at Tower #6, Figure 4, page 13, as the reference, one can observe from Figure 19 that the computed results are always larger than the results from the field tests and the acceleration

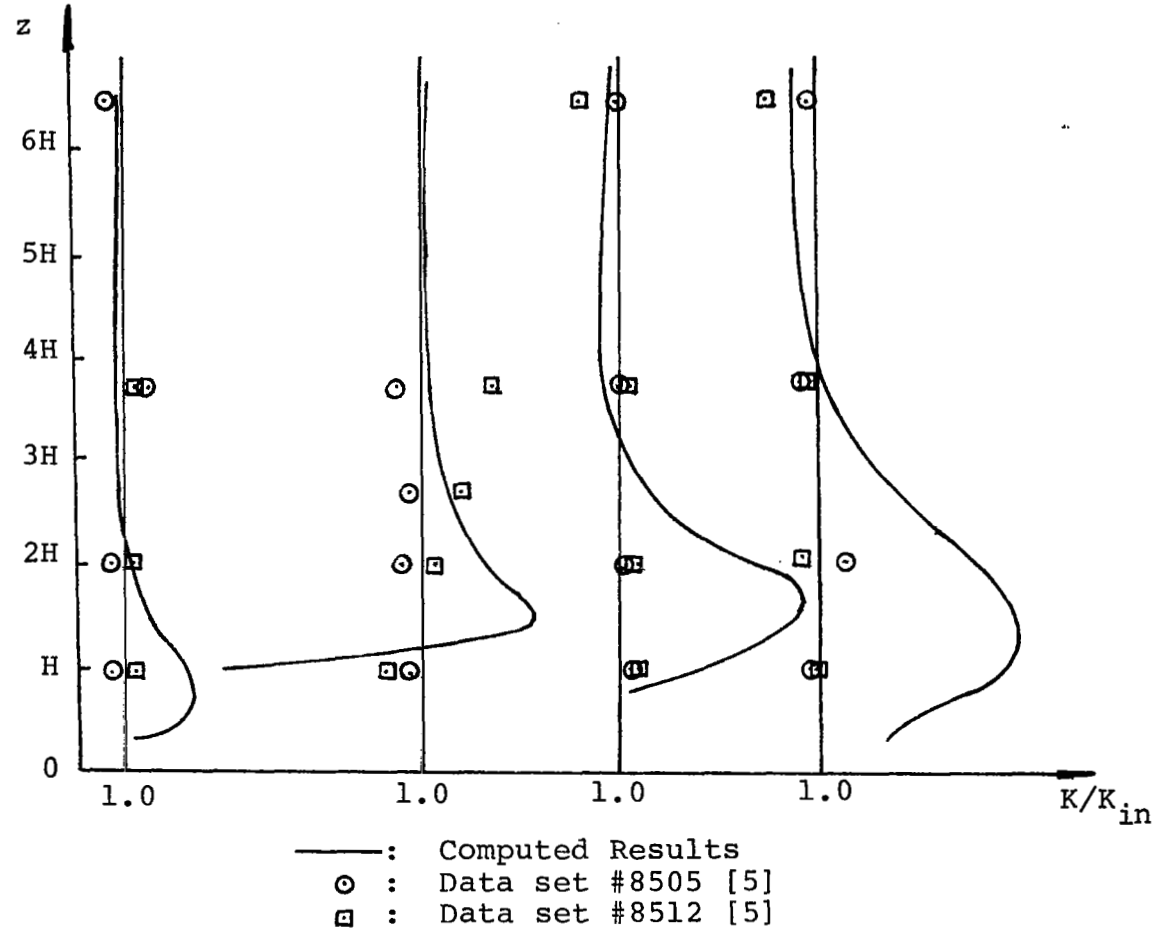

Figure 19. Comparison of the ratio K/K_{in}.

phenomena disappears. The explanation is that the presence of the trees ahead of the block at the field site create a velocity deficit. The velocity measured at Tower #6 [5] is therefore larger than that measured at Tower #1 [5] due to this wake from the trees, and thus the ratio $\frac{u}{u_{in}}$, where u_{in} is measured at Tower #6, will always be lower than the ratio where u_{in} is determined from Tower #1.

Figure 19 shows that the computed turbulence kinetic energy agrees well with the experimental data at locations above four block heights, but does not demonstrate the regions of high turbulence found from computation and wind tunnel experiments. The experimental data (Figure 19) implies that the flow field is always in a local equilibrium state even in the presence of the obstruction which is contradictory to the observation of the wind tunnel tests [28, 29] and to the current results. This may result from the fact that the lateral scale of turbulence in the atmosphere is much greater than that simulated in the wind tunnel. In the numerical model lateral turbulence is, of course, neglected. The rms value of the wind direction measured in the field studies [5] is on the order of ±56 degrees. This is expected to cause some disagreements between the field test data and the two-dimensional computed results.

Figure 20 provides a comparison of the value $\overline{u'w'}$ of the current computed results (calculated by $\overline{u'w'} = \nu_t(\frac{\partial \bar{u}}{\partial z} + \frac{\partial \bar{w}}{\partial x})$) with the results of the field study. In

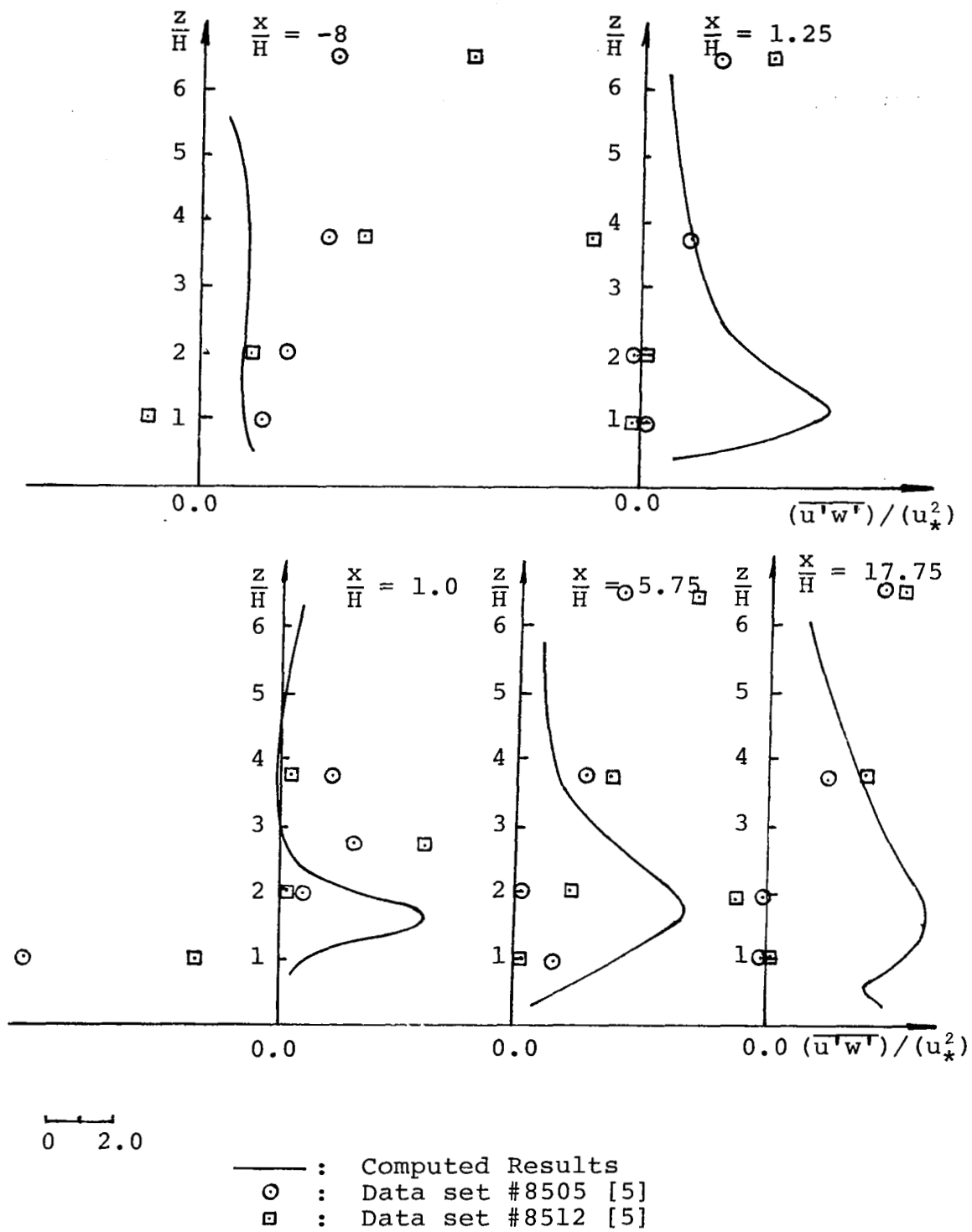

Figure 20. Comparison of the ratio $(\overline{u'w'})/(u_*^2)$.

Figure 20 the values of $\overline{u'w'}$ have been nondimensionalized by dividing by the square of friction velocity, $\frac{\overline{u'w'}}{u_*^2}$. The agreement is very poor. The presence of the trees, which are approximately 3.5 H high and approximately 40 H upstream of the block in the actual field site studied, create a mixing region and are thus believed to produce high values of $\overline{u'w'}$ at heights near that of the tree tops. The current computed results show that the value of $\nu_t\left(\frac{\partial \bar{u}}{\partial z} + \frac{\partial \bar{w}}{\partial x}\right)$ tends to a constant far downstream from the block. This coincides with the concept of a constant shear stress layer for neutrally stable atmospheres (see Chapter II, Section 2).

As mentioned earlier, wind tunnel tests have been conducted which also provide data for comparison with the current computed results. Figure 21 indicates the decay of the mean velocity defect along the wake centerline as computed and as measured in the wind tunnel [28]. Current results coincide almost perfectly with the experimental data. Figure 21 shows that two-dimensional wakes, associated with a long building, having the ratio height/width/depth = 1/8/1, is larger than the three-dimensional wakes associated with short building, H/W/D = 1/2/1. The very good agreement of the computed results with the experimental data for the long block geometry tends to confirm two-dimensionality along the centerline for large aspect ratios.

A comparison of the vertical profiles of the mean velocity defect at selected $\frac{x}{H}$ stations are shown in Figures 22 and 23. These indicate that both the computed results

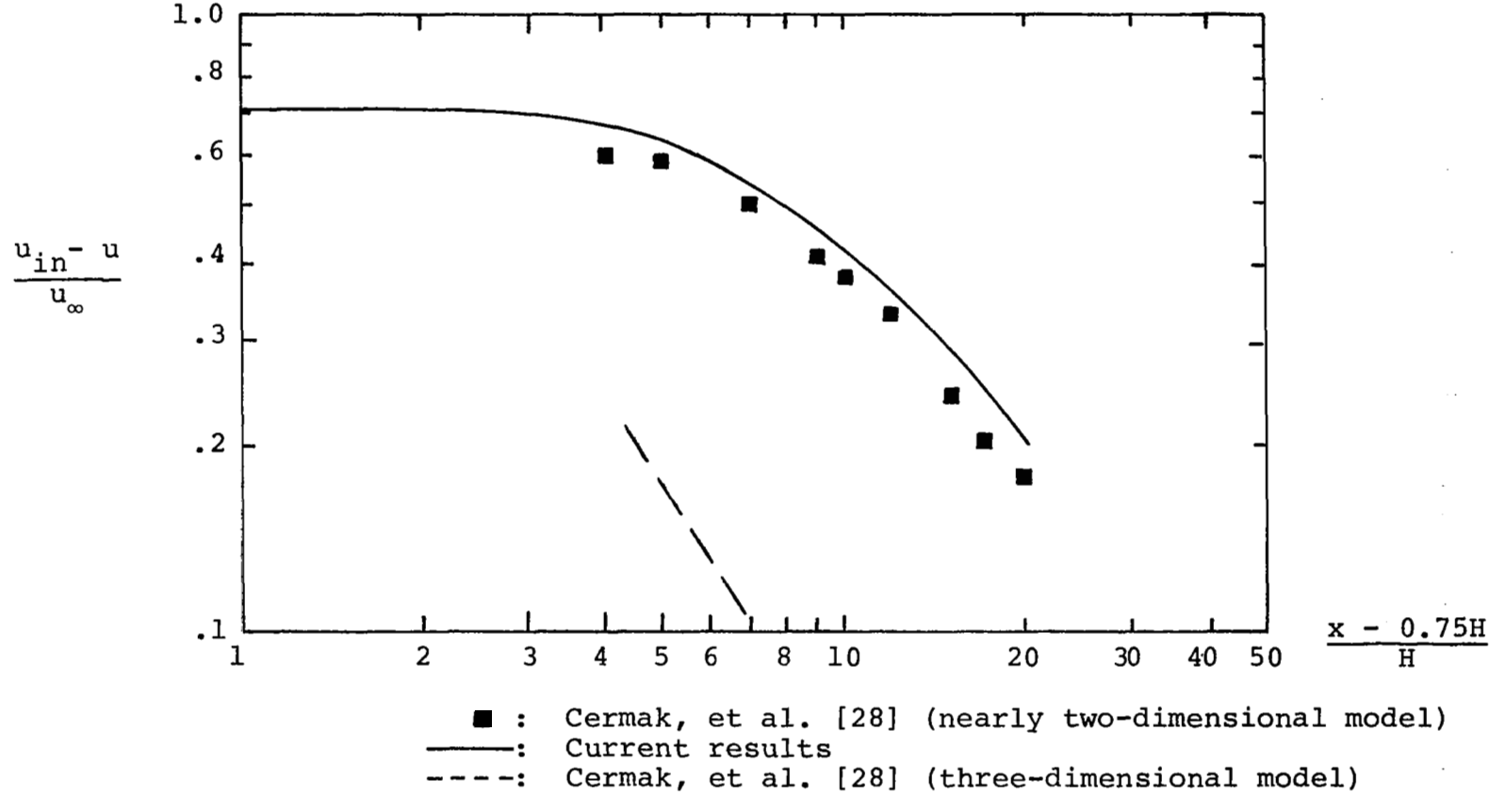

Figure 21. Decay of mean velocity defect along the wake center line.

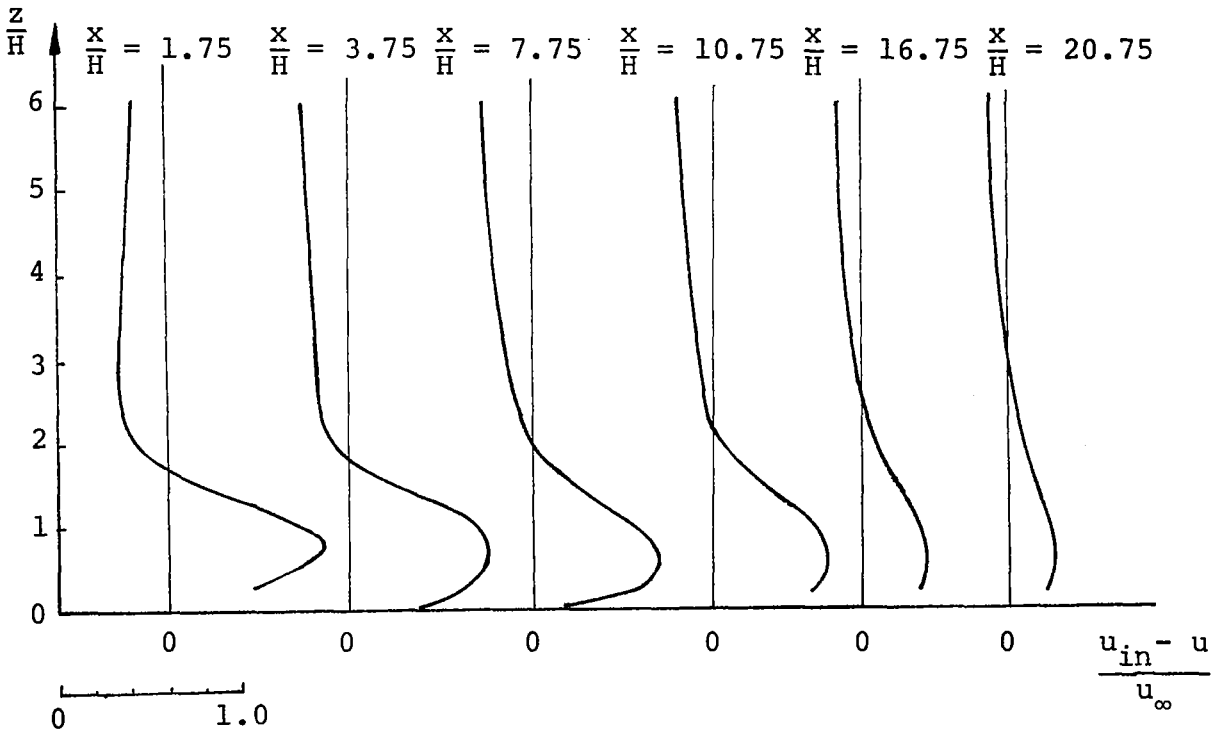

Figure 22. Vertical profiles of mean velocity defect behind the surface block.

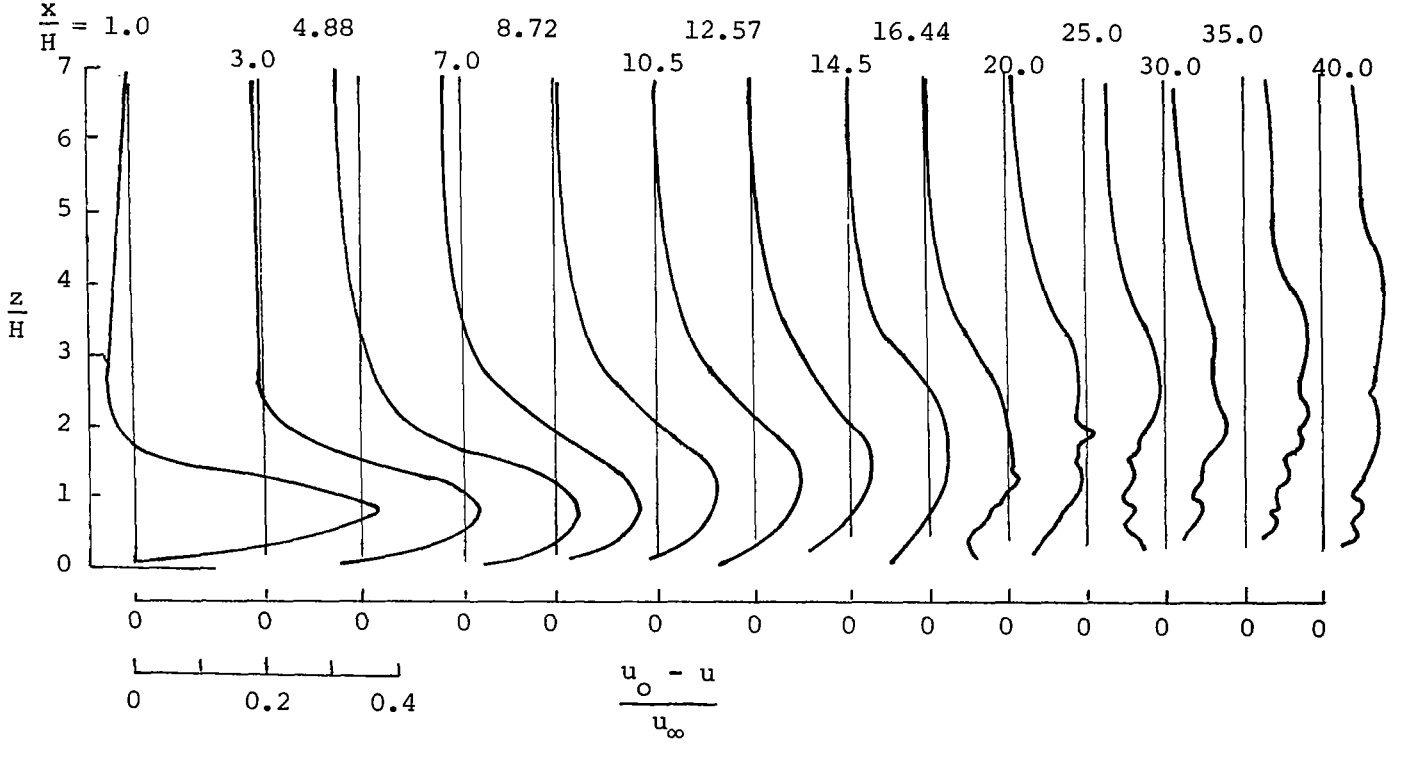

Figure 23. Vertical profiles of mean velocity defect behind model 4 (nearly two-dimensional model) [28].

and the experimental data display a peak value at approximately the height 0.8 H in the vicinity of the block. However, the shear layer appears to diffuse outward slower in the computed results than that in wind tunnel studies. Also the experimental data appear to recover slower than the prediction of this study. The reason is that the flow field, which is considered in the computer study, is specified at 20 H downstream from the block to have zero vertical velocity. Thus, diffusion may be curtailed by the boundary condition.

The magnitude of the measured and computed velocity defects are approximately a factor of two different. However, the data of Figure 21 taken from the same reference for apparently the same test condition do not have this factor of two disagreement. It is therefore believed that the scale given in [28] for Figure 23 is off by a factor of two. If this is the case the computed results show excellent agreement with the experimental results.

Other factors which are expected to cause some disagreement between the wind tunnel data and the theoretical results but not as large as a factor of two difference in magnitude are as follows. The logarithmic velocity profile, which was used as an inlet condition in this study, does not coincide exactly with the power profile used in the wind tunnel study. A comparison of these profiles is given in Figure 24, where the inlet velocity at six block heights is chosen as the reference velocity. The inlet turbulence

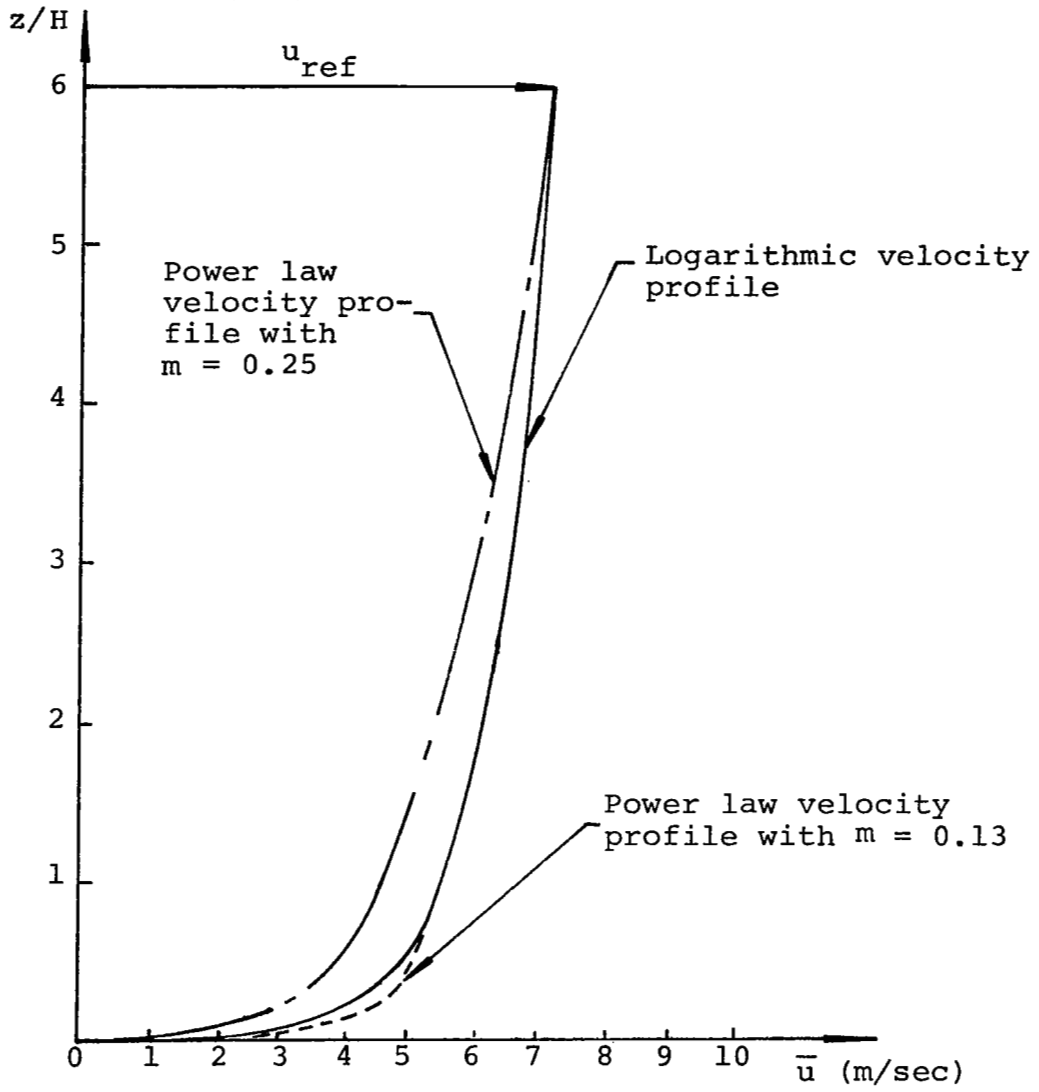

Figure 24. Comparison of logarithmic velocity profile with the power law velocity profile.

kinetic energy is based on the concept of a constant shear layer for a neutrally stable atmospheric boundary layer and thus the gradients of velocity affect the value of the inlet turbulence kinetic energy (Equations 28 and 29). Before discussing this further, the influence of different inlet turbulence kinetic energy levels are discussed. For this purpose, two cases are chosen--Case III and Case IV which assumes $C_{\mu\infty} = C_{D\infty} = 1.0$ and $C_{B\infty} = C_{S\infty} = 1.0$. The effects of increased inlet turbulence kinetic energy can be assessed from Figure 25 which compares the velocity computed for Case III with that for Case IV. From Equation 30, the inlet turbulence kinetic energy for Case III, K_{III}, is larger than that for Case IV, K_{IV}. Inspection of Figure 25 shows that the separation bubble for Case III is slightly larger than that for Case IV. One can conclude that the larger the value of the inlet turbulence kinetic energy the larger the separation bubble. This is not consistent with intuition since large turbulence level would be expected to force reattachment sooner. However, it seems that the ratio $\frac{\Delta K_\ell}{K_{in}}$, where K_ℓ is the local turbulence kinetic energy and K_{in} is the inlet value (see Appendix B), must be considered. Observing Figure 25, one further notes that the velocity defect, $\frac{u_{in} - u}{u_\infty}$ of Case III, is smaller than that of Case IV in the upper region and larger in the lower region. This trend is also believed to be associated with the variation in inlet turbulence kinetic energy. In Reference [28] the upwind turbulence intensity, $\frac{(\overline{u'^2})^{1/2}}{u_\infty}$, is approximately 8%

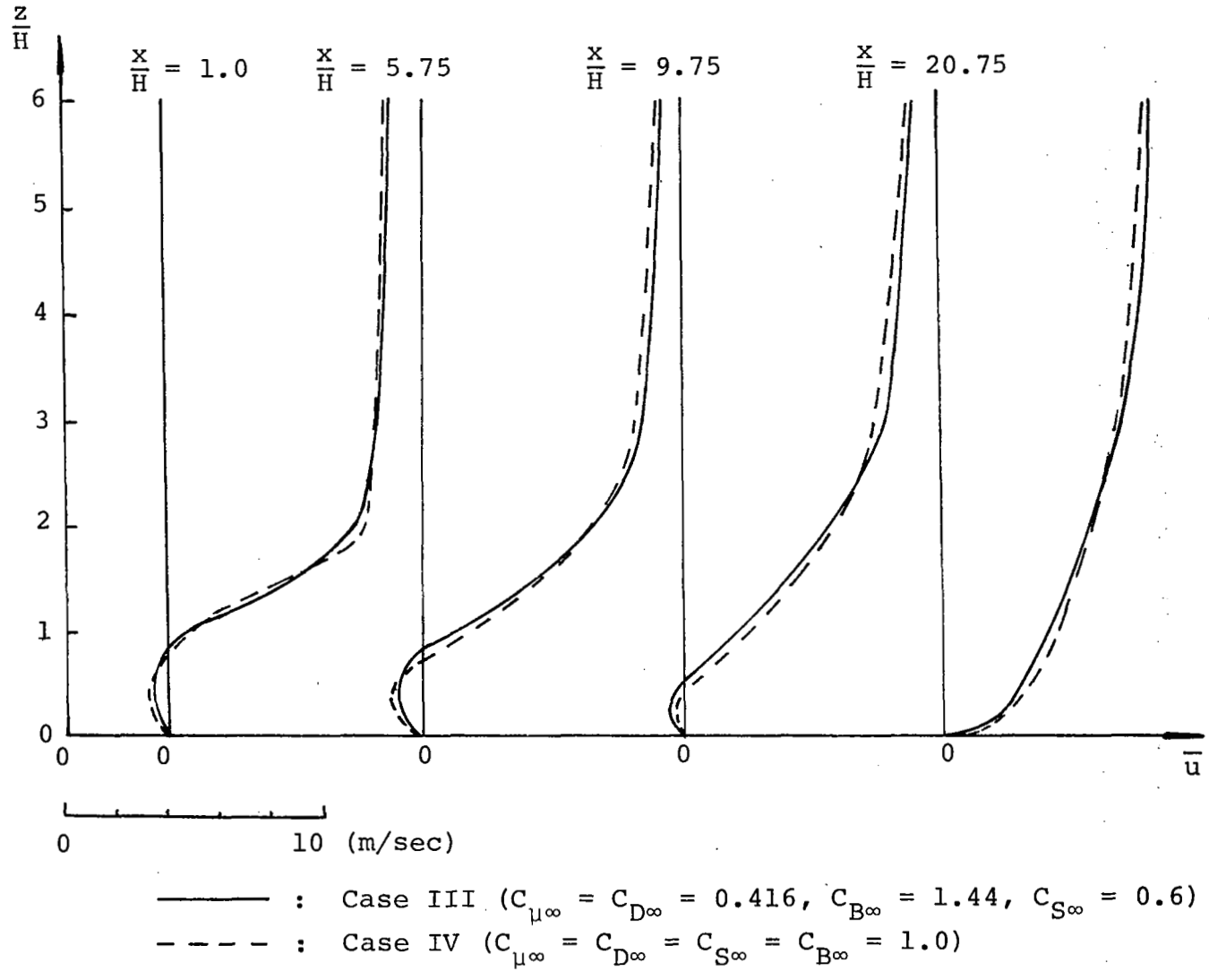

Figure 25. Comparison of velocity profile in the wake region.

which is smaller than the theoretical case investigated in this study, $\frac{(K)^{1/2}}{u_\infty} = 12.5\%$.

If the turbulence were isotropic, $(K)^{1/2} = (\overline{u'^2})^{1/2}$. However, it is expected that the fluctuation velocity in the flow direction is larger than that in the vertical direction so that $\overline{u'^2} > \overline{w'^2}$ and thus

$$\frac{(\overline{u'^2})^{1/2}}{u_\infty} > \frac{(K)^{1/2}}{u_\infty}$$

For example, if $\overline{w^2} = 0.5\ \overline{u'^2}$, then

$$(K)^{1/2} = \left[\frac{1}{2}(\overline{u'^2} + \overline{w'^2})\right]^{1/2} = \left[\frac{1.5}{2}\overline{u'^2}\right]^{1/2}$$

and

$$(\overline{u'^2})^{1/2} = \left[\frac{2}{1.5}\right]^{1/2}(K)^{1/2} > (K)^{1/2}$$

It is therefore to be expected that the velocity defect, $\frac{u_{in} - u}{u_\infty}$, of the wind tunnel studies [28] is larger in the upper region and smaller in the lower region from those predicted by the numerical computation.

Hunt [8] develops a theory for a two-dimensional wake behind a surface block. A comparison of the current results with Hunt's theory is shown in Figure 26. Reference [8] compares the theory with the experimental data from Counihan [8] which is obtained for a power profile with m = 0.125 and shows the data to collapse onto one similarity

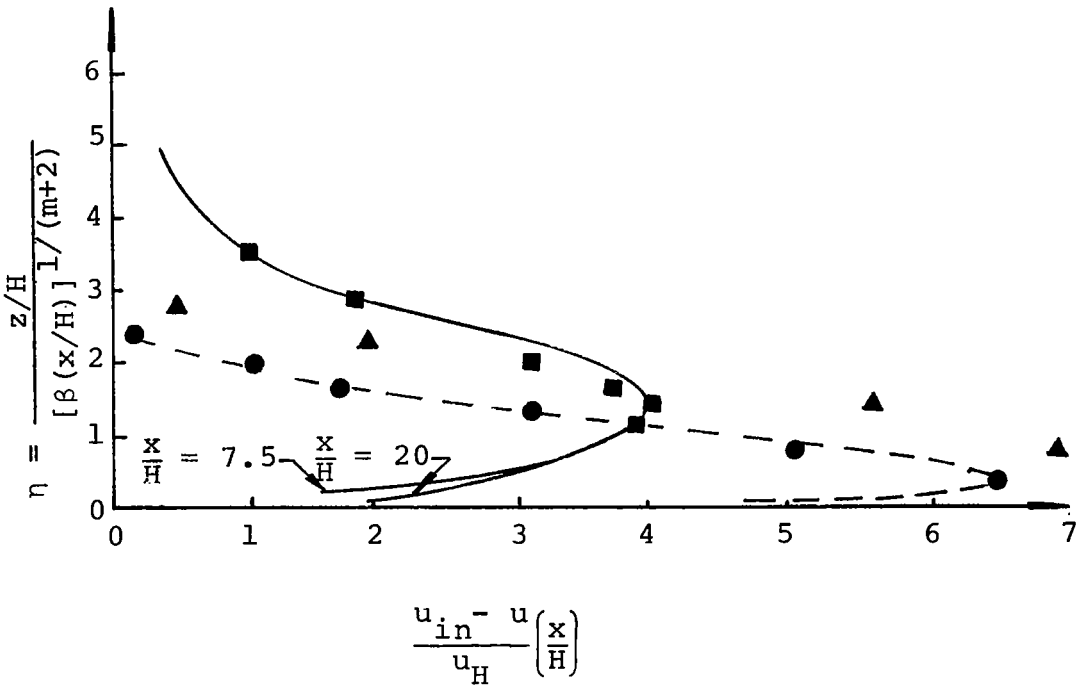

Figure 26. Comparison of Hunt's theory with current computed results (m = 0.125).

curve. The computed results here, however, do not show the same tendency to collapse onto a single curve as suggested by Hunt's theory. Reference [28] also found that their data did not fall on a similarity curve. It should be noted that the computed results along the approximate center line of the mixing layer at $z \approx 1.25$ H agree relatively well with Hunt's theory.

Reference [8], whose data agree with Hunt's theory well, shows a separation bubble which extends to $x/H = 6.0$ and is considerably smaller than that of the computed results for which the reattachment point occurs at $x/H = 11.5$. This difference is believed to be a reason why the computed results reported in this study depart from Hunt's theory.

It is useful to investigate the character of the computed shear layer shed from the leading edge of the building. Many experiments [14, 29, 30] have shown the velocity in the shear layer to be governed by the erf function profile. In this study, the upper boundary of the mixing region is defined as $u/u_\infty = 1.0$, where u_∞ is taken as the inlet velocity at the upper boundary of the region (i.e., $u_\infty = \frac{u_*}{k} \ln \frac{6H + z_o}{z_o}$). The line $\frac{u}{u_\infty} = \frac{1}{2}$ as conventionally done, treated as the jet axis of the mixing layer theory, $\frac{u}{u_\infty} = \frac{1}{2}(1+\text{erf } \xi)$ where $\xi = \sigma \frac{y}{x}$, y is measured from jet-axis and σ is a constant to be determined. Figure 27 indicates the jet-axis and upper boundary of mixing layer. The wedge fence model [29] gives a higher upper mixing

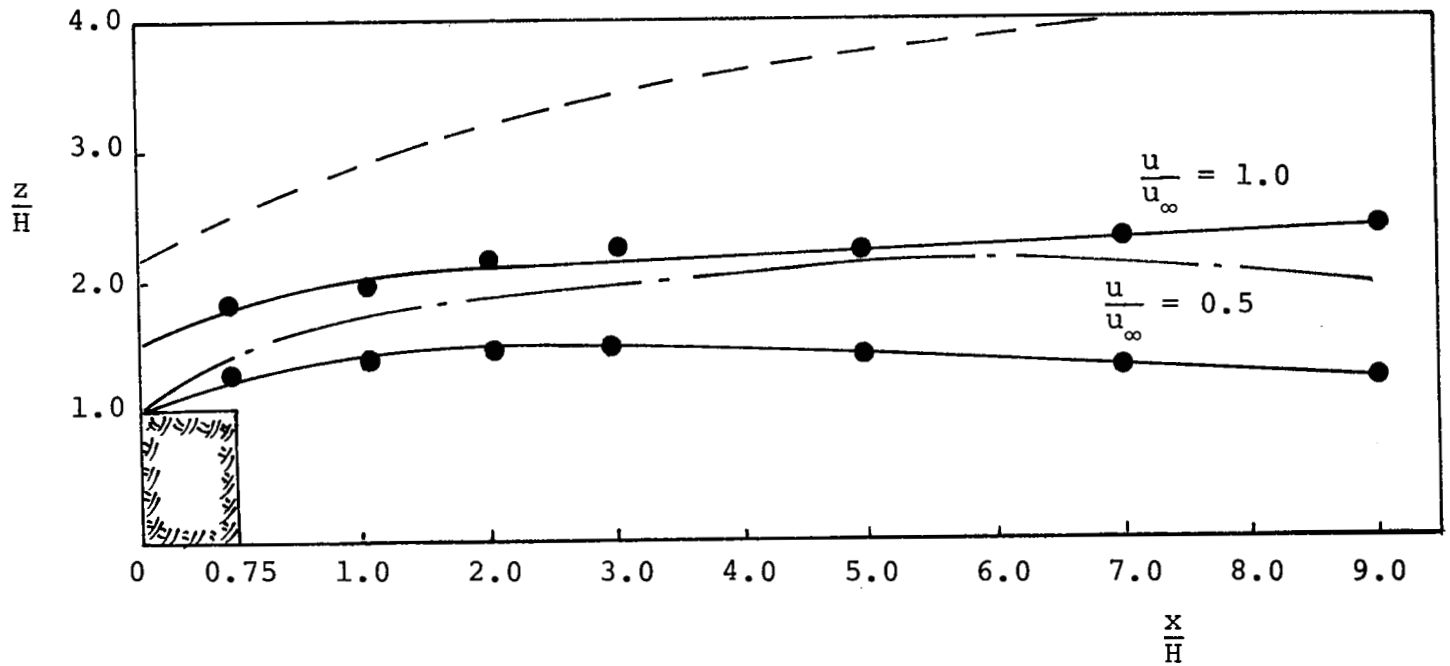

Figure 27. Upper mixing boundary and jet-axis.

boundary and a higher jet-axis than the computed results for the rectangular block. This is reasonable in that the wake region of the fence extends much higher than that of a forward facing step and the rectangular block represents an intermediate case. The height of the wake region is obviously a function of the recirculating flow and resulting pressure build-up for the different geometries. It should be noted that the current computed results of a wake approximately 2 H in height coincides with the results of the smoke trace study carried out in Reference [5].

A comparison of the mixing layer theory with the current computed results and the values of the computed spreading parameter, σ, are shown in Figure 28. Figure 29 is a plot of the spreading parameter σ with respect to x/H. The results from the wedge fence model [29] is also shown in Figure 29. The explanation of the difference between the computed results and the experimental data could be that the value of σ is dependent on the geometry of the bluff body from which separation occurs. Evidence that σ depends on geometry is given in Reference [30]. Another possible reason for the difference between the computed σ and the measured values of [29] is that the over prediction of the turbulence kinetic energy in the flow field may force the flow to bend to the ground early and make the mixing region smaller than that observed in Reference [29].

Figure 30 shows the computed turbulent properties $\frac{K}{u_\infty^2}$ and $\frac{\tau_t}{u_\infty^2}$ (or $\nu_t(\frac{\partial \overline{u}}{\partial z} + \frac{\partial \overline{w}}{\partial x})$). It is observed that the peak

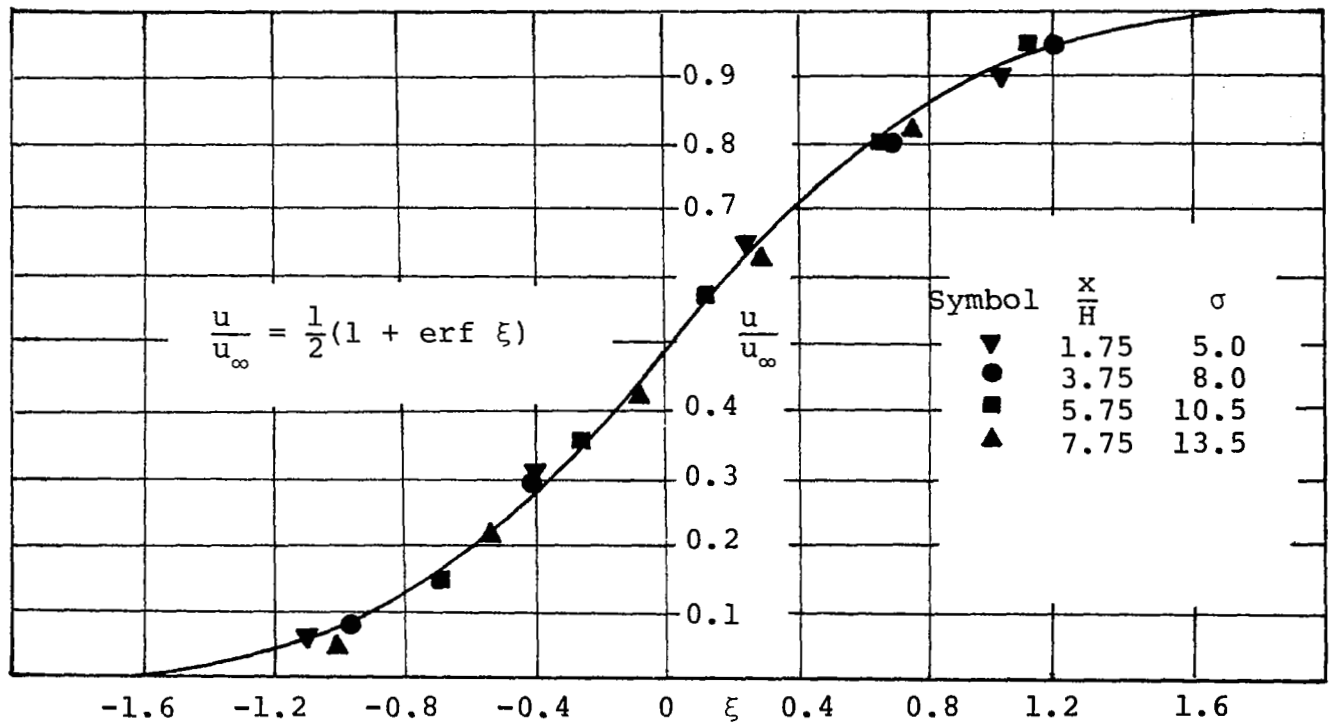

Figure 28. Comparison of mixing layer theory and current computed results.

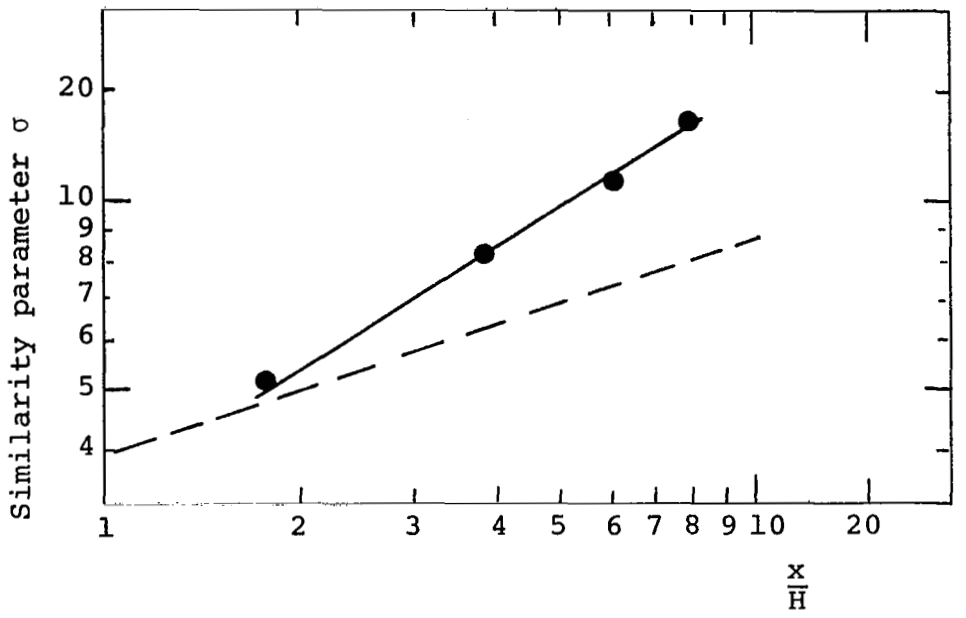

Figure 29. Variation of similarity parameter with the ratio x/H.

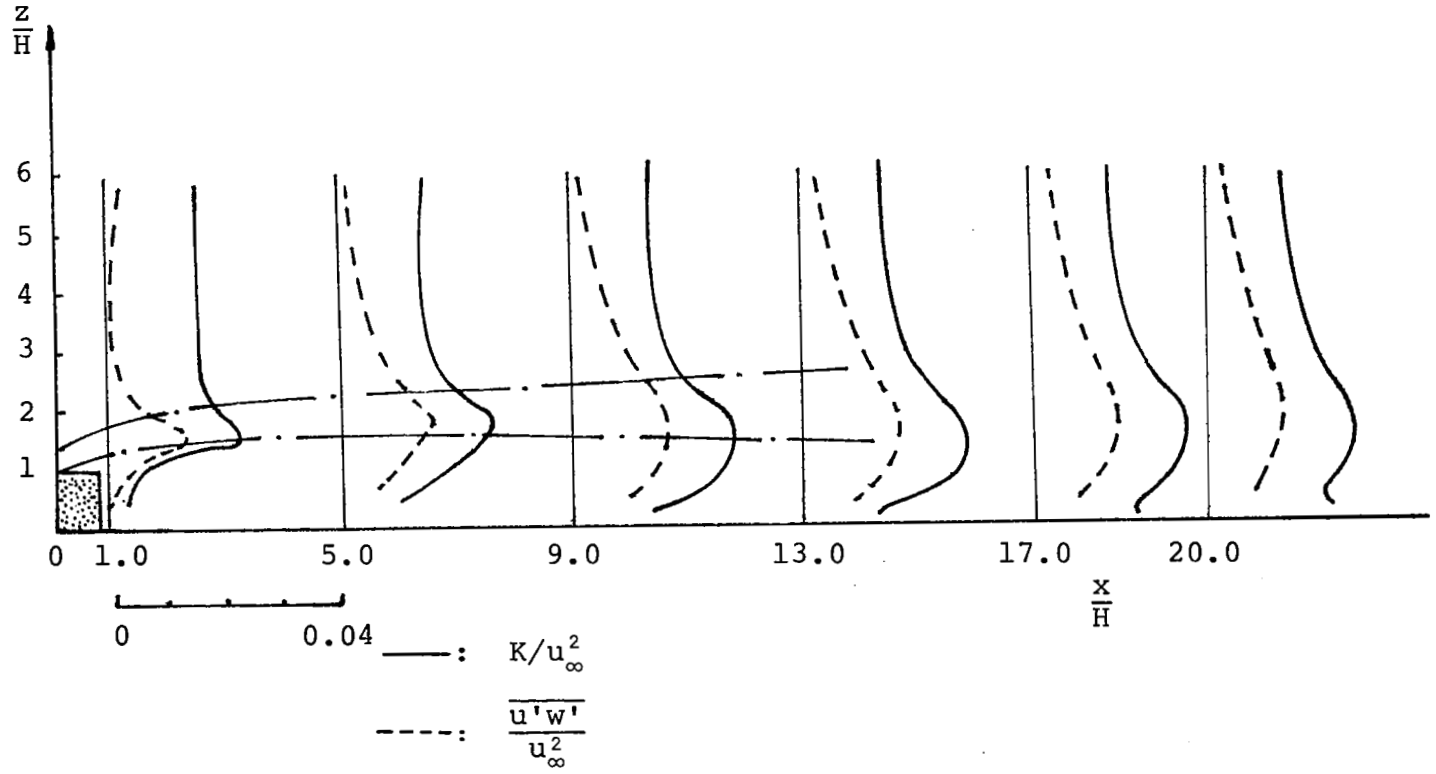

Figure 30. Turbulence kinetic energy and turbulent shear stress behind a surface block.

value turbulence kinetic energy occurs along the axis of mixing layer and then approaches a constant outside the upper mixing boundary. The former phenomena coincides with the observation in Reference [29] for the turbulence intensity which is proportional to the turbulence kinetic energy (see Figure 31), but the turbulence intensity of [29] approaches zero rather than a constant as in Figure 30. The explanation is that the flow field considered in this study is a neutrally stable atmospheric layer which possesses constant shear stress in the undisturbed case and thus has constant turbulence kinetic energy.

The turbulent shear stress in Figure 30 has a different sign from that in Figure 31. This is simply because of the sign convention chosen for displaying the data.

7. CONCLUSIONS

The present approach of solving the ensemble averaged two-dimensional incompressible turbulent Navier-Stokes equations as applicable to a neutrally stable atmospheric flow over a two-dimensional block has been shown to yield results in agreement with the experimental findings. The two equation model (K - ℓ model) of turbulence has been demonstrated to produce realistic results in the recirculation flow field reported in this study.

The influence of the coefficients' ratio on the turbulence kinetic energy and turbulence length scale of

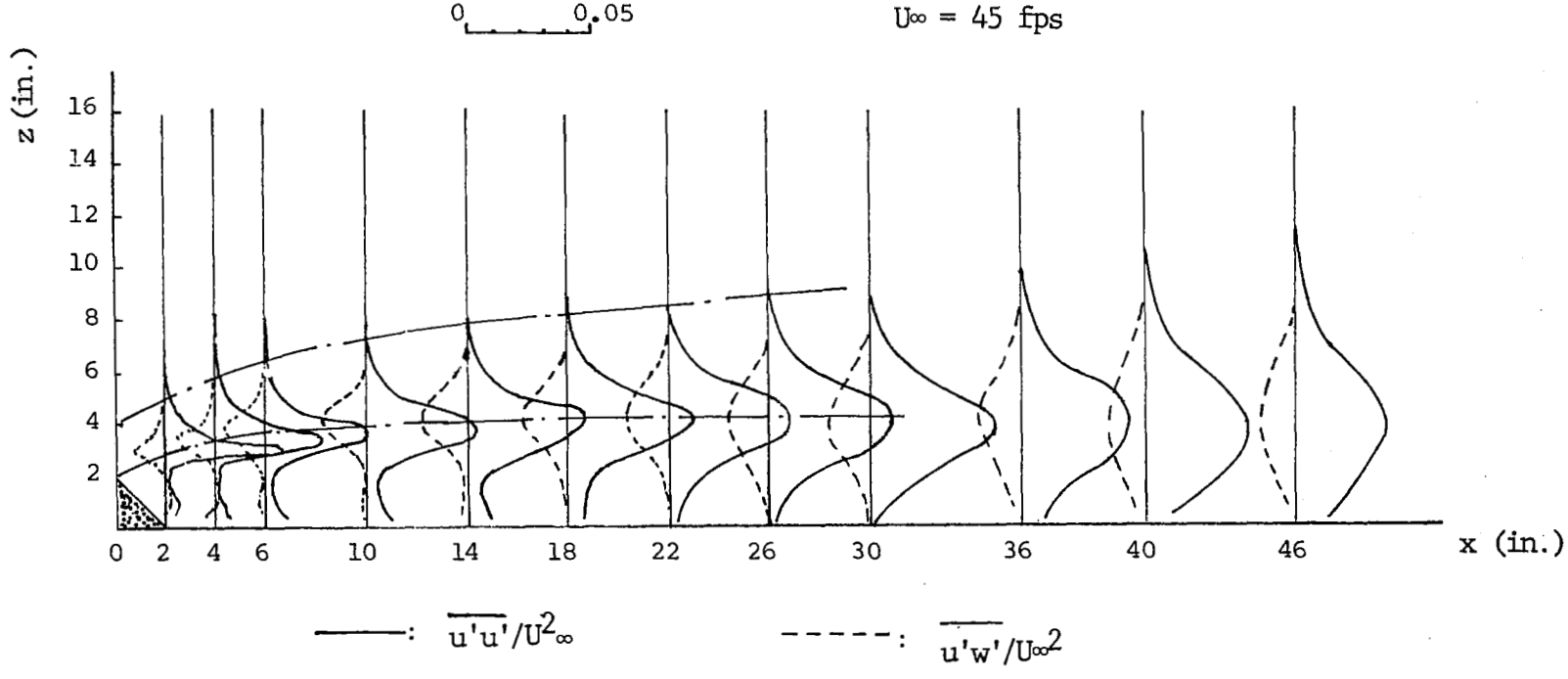

Figure 31. Turbulent components behind the wedge fence 2 in. x 2 in. [29].

the flow field of interest and on the predicted results have been computationally investigated, and a set of constants has been determined for the problem under study. The results of the study show that the ratio $\frac{C_{S\infty}}{C_{D\infty}\ C_{B\infty}}$ has a value close to unity.

BIBLIOGRAPHY

1. Frost, Walter. "Review of Data and Prediction Techniques for Wind Profiles Around Manmade Surface Obstructions," AGARD-CP-140, Section 4, May, 1973.

2. Chang, P. K. Separation of Flow. New York: Pergamon Press, 1970.

3. Colmer, M. J. "Some Full Scale Measurements of the Flow in the Wake of a Hangar," ARC-CO-1166, H.M.S.O., 1971.

4. Hansen, A. C., J. A. Peterka, and J. E. Cermak. "Wind Tunnel Measurements in the Wake of a Simple Structure in a Simulated Atmospheric Flow," NASA-CR-2540, April, 1974.

5. Frost, W., and A. M. Shahabi. "A Field Study of Wind over a Simulated Block Building," Report prepared under NSF Contract No. GK-22902, September, 1975.

6. Lemberg, R. "On the Wakes behind Bluff Bodies in a Turbulent Boundary Layer," Report BLWT-3-73, University of Western Ontario, London, Canada, 1973.

7. Muller, T. J., and J. M. Roberson. "A Study of the Mean Motion and Turbulence Downstream of a Roughness Element," Developments in Theoretical and Applied Mechanics. New York: Plenum Press, 1963.

8. Hunt, J. C. R., P. S. Jackson, and J. Counihan. "Wakes behind Two-Dimensional Surface Obstacles in Turbulent Boundary Layers," Journal of Fluid Mechanics, 64(Part 3):529-540, 1974.

9. Townsend, A. A. "Self-Preserving Flow inside a Turbulence Boundary Layer," Journal of Fluid Mechanics, 22:773-797, 1965.

10. Plate, E. J. "Aerodynamics of Shelter Belts," Agricultural Meteorology, 8:203-222, 1971.

11. Gosman, A. D., W. M. Pun, A. K. Runchal, D. B. Spalding, and M. Wolfshtein. Heat and Mass Transfer in Recirculating Flows. New York: Academic Press, Inc., 1973.

12. Bradshaw, P., and F. Y. F. Wong. "The Reattachment and Relaxation of Turbulent Shear Layer," Journal of Fluid Mechanics, 52:113-135, March, 1972.

13. Frost, W., and J. Bitte. "Atmospheric Flow over Two-Dimensional Bluff Surface Obstructions," Report prepared under NASA Contract No. NAS8-29584, 1975.

14. Frost, W., and U. K. Kaul. "Turbulent Atmospheric Flow over a Backward-Facing Step," Report prepared under NASA Contract No. NAS8-29584.

15. Blackadar, A. K. "The Vertical Distribution of Wind and Turbulent Exchange in a Neutral Atmosphere," Journal of Geophysical Research, 67:3095-3102, April, 1962.

16. Lettau, H. H. "Wind Profile, Shear Stress and Geostrophic Drag Coefficients in the Atmospheric Surface Layer," Advances in Geophysics. New York: Academic Press, 1962.

17. Frost, W., J. R. Maus, and W. R. Simpson. "A Boundary Layer Approach to the Analysis of Atmospheric Motion over a Surface Obstruction," Report prepared under NASA Contract No. CR-2182 by The University of Tennessee Space Institute, Tullahoma, Tennessee, January, 1973.

18. Panofsky, H. A. "The Atmospheric Boundary Layer Below 150 Meters," Annual Review of Fluid Mechanics, Vol. 6, 1974.

19. Wyngaard, J. C. "On Surface-Layer Turbulence," Workshop on Micrometeorology, Chapter 3, published by the American Meteorological Society, 1973.

20. Launder, B. E., A. Morse, W. Rodi, and D. B. Spalding. "Prediction of Free Shear Flows--A Comparison of the Performance of Six Turbulence Model Free Turbulent Shear Flow," Vol. I, National Aeronautics and Space Administration SP-321, July, 1972.

21. Launder, B. E., and D. B. Spalding. Mathematical Models of Turbulence. London and New York: Academic Press, 1972.

22. Wolfshtein, M. "Convection Processes in Turbulent Impinging Jets." Ph.D. dissertation, Imperial College of Science and Technology Mechanical Engineering Department Report SF/R/I/2, London, England, November, 1967.

23. Roache, P. J. Computational Fluid Dynamics. Hermosa Publishers, 1972.

24. Rodi, W., and D. B. Spalding. "A Two-Parameter Model of Turbulence and Its Application to Free Jets," Wärm-und Stoffübertragung, 3(Number 2):85-95, 1970.

25. Ng, K. H., and D. B. Spalding. "Turbulence Model for Boundary Layers Near Walls," The Physics of Fluids, 15(Number 1):20-30, January, 1972.

26. Frost, W., and W. L. Harper. "Analysis of Atmospheric Flow over a Surface Protrusion Using the Turbulence Kinetic Energy Equation with Reference to Aeronautical Operating Systems," Report prepared under NASA Contract No. NASA CR-2630, December, 1975.

27. Tani, I., M. Iuchi, and H. Komoda. "Experimental Investigation of Flow Separation Associated with a Step or a Groove," Aeronautical Research Institute Report No. 364, University of Tokyo, April, 1961.

28. Cermak, J. E., J. A. Peterka, and H. G. C. Woo. "Wind Tunnel Measurements in the Wakes of Structures," Report being prepared for NASA under Contract No. NAS8-29583.

29. Chang, Shih-Cheng. "Velocity Distributions in the Separated Flow behind a Wedge Shaped Model Hill," Report prepared under U.S. Army Research Grant DA-AMC-28-043-G30, March, 1966.

30. Tanner, M. "Theoretical Prediction of Base Pressure for Steady Base Flow," Progress in Aerospace Sciences, D. Küchemann, editor. Vol. 14. New York: Pergamon Press, Inc., 1973.

APPENDIXES

APPENDIX A

COEFFICIENT CONSTANTS OBTAINED FROM BOUNDARY LAYER APPROACH

Considering the transport equations of turbulence kinetic energy and turbulence length scale, e.g., Equations 18 and 21, and taking the boundary layer approach, Equations 18 and 21 are reduced to

$$\rho w \frac{\partial K}{\partial z} = \frac{\partial}{\partial z}\left(\mu_{eff} \frac{\partial K}{\partial z}\right) + \mu_t \left(\frac{\partial u}{\partial z}\right)^2 - C_D \rho \frac{K^{3/2}}{\ell} \tag{A-1}$$

and

$$\rho w \frac{\partial \ell}{\partial z} = \frac{\partial}{\partial z}\left(\mu_{eff} \frac{\partial \ell}{\partial z}\right) - \mu_t \left(\frac{\partial u}{\partial z}\right)^2 \frac{\ell}{K} \cdot C_B + C_s \rho K^{1/2} \tag{A-2}$$

Introducing the concept of a constant shear stress layer such that turbulence kinetic energy is constant and of the turbulence Reynolds number, $R_t = \frac{\mu_t}{C_{\mu\infty} \cdot \mu}$, is very large, Equation 24. Equation A-1 simplifies to

$$\mu_t \left(\frac{\partial u}{\partial z}\right)^2 = C_D \rho \frac{K^{3/2}}{\ell} \tag{A-3}$$

Thus the production and dissipation of turbulence kinetic energy are in equilibrium.

Wind profile in surface layer is described as Equation 1, such that

$$\left(\frac{\partial u}{\partial z}\right) = \frac{u^*}{k} \cdot \frac{1}{z + z_o} = \frac{u^*}{\ell} \tag{A-4}$$

where $\ell = k(z + z_o) = 0.4(z + z_o)$.

Substitute into Equation A-3

$$C_\mu \cdot u_*^2 = C_D \cdot K \tag{A-5}$$

together with Equation 30

$$C_D = C_\mu^3 \tag{A-6}$$

In the case of negligible convection effect, e.g., vicinity to the wall, Equation A-2 is reduced to

$$\frac{\partial}{\partial z}\left(C_\mu \rho K^{1/2} \ell \frac{\partial \ell}{\partial z}\right) + C_s K^{1/2} \rho - \mu_t \left(\frac{\partial u}{\partial z}\right)^2 \frac{\ell}{k} \cdot C_B = 0 \tag{A-7}$$

so that

$$k^2 \cdot C_\mu + C_S - C_D \cdot C_B = 0 \tag{A-8}$$

or

$$C_B = \frac{k^2 \cdot C_\mu}{C_D} + \frac{C_S}{C_D} \tag{A-9}$$

On the other hand, one can find a relationship between coefficient constants in equilibrium state from Equation A-7. That is

$$C_S K^{1/2} \rho = \mu_t \left(\frac{\partial u}{\partial z}\right)^2 \frac{\ell}{K} \cdot C_B \tag{A-10}$$

or

$$\frac{C_S}{C_B C_D} = 1.0 \qquad \text{(A-11)}$$

Based on the consideration of boundary layer approach, one has already obtained:

1. Equation A-6 together with Equation A-9 is valid for the case in which convection effect can be neglected.
2. Equation A-6 together with Equation A-11 is available for the equilibrium state.

It is necessary to mention that those results are obtained by the assumption $\frac{\partial u}{\partial x} = 0$ so that it is not acceptable in a complicated flow situation, e.g., recirculation flow. The turbulence length scale is assumed to obey Prandtl mixing length hypothesis vicinity to the wall.

APPENDIX B

PREDICTION OF THE SIZE OF SEPARATION BUBBLE BEHIND A BLOCK

The local turbulence kinetic energy, K_ℓ, may be denoted by the following:

$$K_{\ell,2} = K_{\ell,1} + K_C - K_D \tag{B-1}$$

where the subscripts "1," "2," "C" and "D" denote the upstream condition, the downstream condition, the production and the dissipation of the local turbulence kinetic energy, respectively. According to Equation B-1, the following equation is obtained:

$$\frac{K_{\ell,2} - K_{\ell,1}}{K_{in}} = \frac{K_D}{K_{in}}\left(\frac{K_C}{K_D} - 1\right)$$

One can define a ratio R by the following:

$$R = \frac{K_{\ell,2} - K_{\ell,1}}{K_{in}} = \frac{\Delta K_\ell}{K_{in}} \tag{B-2}$$

One can also denote the relationship of the ratio R of two different cases, say case I and case II, as follows:

$$\frac{R_I}{R_{II}} = \frac{(K_D)_I}{(K_D)_{II}} \cdot \frac{(K_{in})_{II}}{(K_{in})_I} \cdot \frac{\left(\frac{K_C}{K_D} - 1\right)_I}{\left(\frac{K_C}{K_D} - 1\right)_{II}} \tag{B-3}$$

According to dimensional analysis (refer to Equation 20), one denotes

$$K_D = C_D \rho \frac{K_\ell^{3/2}}{\ell} \tag{B-4}$$

Substituting Equation B-4 into Equation B-3, one obtains:

$$\frac{R_I}{R_{II}} = \frac{(C_D)_I (K)_I^{3/2}}{(C_D)_{II} (K)_{II}^{3/2}} \cdot \frac{\ell_{II}}{\ell_I} \cdot \frac{(K_{in})_{II}}{(K_{in})_I} \cdot \frac{\left(\frac{K_C}{K_D} - 1\right)}{\left(\frac{K_C}{K_D} - 1\right)} \tag{B-5}$$

Assuming $\ell_I \doteqdot \ell_{II}$ for the same inlet boundary condition of the turbulence length scale and assuming the ratio $\frac{K_C}{K_D}$ is the same for the same geometry array of the flow field, Equation B-5 is simplified in the following:

$$\frac{R_I}{R_{II}} = \frac{(C_D)_I}{(C_D)_{II}} \cdot \frac{(K_\ell)_I^{3/2}}{(K_\ell)_{II}^{3/2}} \cdot \frac{(K_{in})_{II}}{(K_{in})_I} \tag{B-6}$$

Based on Equation B-6, the following discussions are given.

Discussion I:

If the inlet boundary conditions of two cases are the same, it is reasonable to assume the local turbulences of these two cases are always in the same order. Basing on this assumption, Equation B-6 is simplified as follows.

$$\frac{R_I}{R_{II}} \doteqdot \frac{C_{DI}}{C_{DII}} \tag{B-7}$$

If C_{DI} is larger than C_{DII}, one expects R_I is larger than R_{II}. Due to the definition of the ratio R, one may argue that the larger the ratio R the larger the turbulence tendency in the flow field. Basing on this argument and the fact that the laminar flow always creates a larger separation bubble than the turbulent one, one concludes that the larger the C_D value the smaller the separation bubble for the cases which possess the same inlet turbulence kinetic energy.

In this study, it has been discovered that the separation bubble extends approximately to 6 H behind the block for the case $C_D = 1.0$ and approximately 11.5 H for the case $C_D = 0.416$.

Discussion II:

Due to the reason that the problem concerned in this study is a boundary-value problem (see Chapter II, Section 6), one may argue that the larger inlet turbulence kinetic energy always creates the larger local value at a specified location in the flow field. According to Equation 30, one expects that the larger C_μ value the larger inlet turbulence kinetic energy. For the cases which possess the same ratio $\frac{C_\mu}{C_D}$ but have different inlet turbulence kinetic energy, one expects that the larger inlet turbulence kinetic energy the larger value of C_D. Considering Equation B-6, assuming $K_{in,II} > K_{in,I}$, and basing on the arguments stated above, one expects that $C_{D,II} > C_{D,I}$ and $K_{\ell,II} > K_{\ell,I}$ and thus the

magnitude of R_I to compare with that of R_{II} is ambiguous (Equation B-6). In this study the $\frac{C_\mu}{C_D}$ ratio is chosen to be unity. The separation bubble extends to 11.5 H behind the block for the case $C_D = 0.416$ and extends to approximately 11.0 H for the case $C_D = 1.0$. One may conclude that the size of the separation bubble does not change very much even though the variation of C_D value is large if the ratio $\frac{C_\mu}{C_D}$ is kept constant.

1. REPORT NO.	2. GOVERNMENT ACCESSION NO.	3. RECIPIENT'S CATALOG NO.
NASA CR-2926		

4. TITLE AND SUBTITLE	5. REPORT DATE
Neutrally Stable Atmospheric Flow over a Two-Dimensional Rectangular Block	November 1977
	6. PERFORMING ORGANIZATION CODE
7. AUTHOR(S)	8. PERFORMING ORGANIZATION REPORT #
Chih Fang Shieh, Walter Frost, and Juergen Bitte	M-242
9. PERFORMING ORGANIZATION NAME AND ADDRESS	10. WORK UNIT NO.
The University of Tennessee ~~Space Institute~~ Tullahoma, Tennessee	11. CONTRACT OR GRANT NO. NAS8-29584
	13. TYPE OF REPORT & PERIOD COVERED Contractor
12. SPONSORING AGENCY NAME AND ADDRESS National Aeronautics and Space Administration Washington, D. C. 20546	14. SPONSORING AGENCY CODE

15. SUPPLEMENTARY NOTES

Prepared under the technical monitorship of the Atmospheric Sciences Division, Space Sciences Laboratory, NASA/Marshall Space Flight Center

16. ABSTRACT

The phenomena of atmospheric flow over a two-dimensional surface obstruction such as a building (modeled as a rectangular block) are analyzed by an approach using the Navier-Stokes equations with a two-equation model of turbulence; i. e., two additional transport equations for turbulence kinetic energy and turbulence length scale.

In this approach the partial differential equations for the vorticity, stream function, turbulence kinetic energy, and turbulence length scale are solved by a finite-difference technique. The predicted results are in agreement with the limited experimental data available.

The current computed results show that the separation bubble originates from the upper front corner of the block and extends approximately 11.5 block heights behind the block. The decay of the mean velocity along the wake center line coincides almost perfectly with the experimental data. The vertical profiles of the mean velocity defect are also in reasonable agreement with the wind tunnel results. The velocity profiles in the mixing region are shown to agree with the error function profile typically found in the shear layer. The details of the behavior of the turbulence kinetic energy and the turbulence length scale are also given and are discussed in this study.

17. KEY WORDS	18. DISTRIBUTION STATEMENT
	Category: 47

19. SECURITY CLASSIF. (of this report)	20. SECURITY CLASSIF. (of this page)	21. NO. OF PAGES	22. PRICE
Unclassified	Unclassified	107	$5.50

For sale by the National Technical Information Service, Springfield, Virginia 22161

NASA-Langley, 1977